

1 **Title:** Effects of boundary hydraulics, dissolved oxygen, and dissolved organic carbon on growth
2 and death dynamics of aerobic microbes in riverbed dune-induced hyporheic zones

3

4 **Authors:** Hector Monterroso¹, Mark A. Widdowson¹, W. Seth Lotts¹, Kyle Strom, and Erich T.
5 Hester¹

6

7 ¹Department of Civil and Environmental Engineering, 200 Patton Hall, 750 Drillfield Drive,
8 Virginia Tech, Blacksburg, Virginia 24061 USA

9

10 Corresponding Author: Erich T. Hester, ehester@vt.edu

11

12

13 **Abstract**

14 Surface and groundwater interact in the hyporheic zone beneath and adjacent to rivers in the
15 presence of a diverse microbial community. Heterotrophic bacteria mediate a range of
16 environmentally important reactions, yet few studies have quantified bacterial growth and death
17 dynamics in the hyporheic zone, and none have systematically analyzed their response to
18 variations in hydraulic or chemical conditions. We used MODFLOW and SEAM3D to simulate
19 hydraulics; dissolved oxygen (DO) and dissolved organic carbon (DOC) transport; and aerobic
20 microbial metabolism, growth, and death in hyporheic zones induced by riverbed dunes. We ran
21 simulations both with and without growth/death processes, and varied hydraulic parameters and
22 DO/DOC boundary concentrations. Microbial biomass reached steady state ($t=3$ days) in every
23 simulation, at which time there was greater biomass and DOC biodegradation rates in the
24 hyporheic flowcell (300% and 85% higher for the base case, respectively) when accounting for
25 microbial growth dynamics. This occurred as microbial biomass tailored its spatial distribution
26 to the availability of DO and DOC, demonstrating the importance of simulating growth/death
27 processes. Biomass generally increased with hyporheic flow cell area as upwelling groundwater
28 decreased. When varying surface water DO and DOC source concentrations relative to the base
29 case, the greatest effect on biomass occurred when increasing DOC and decreasing DO. We
30 determined minimum DO and DOC steady-state concentrations required for microbial growth,
31 but the minimums were not absolute or related by stoichiometry. Increasing DOC created a

32 smaller area of microbes with higher concentrations relative to the base case. Increasing DO
33 slightly increased the area occupied by microbes while keeping the total biomass nearly constant.
34 Overall, microbial growth and death dynamics depend on DO and DOC availability in the
35 hyporheic zone, which is dependent on DOC/DO boundary concentrations and hyporheic flow
36 paths, and in turn the hydraulic interaction between surface water and groundwater.

37

38 **Keywords**

39 hyporheic exchange, streambed, rivers, biogeochemistry, aerobic respiration

40

41

42 **1. Introduction**

43 The hyporheic zone is the zone of interaction of surface water (SW) and groundwater (GW)
44 beneath and adjacent to streams and rivers (Jones and Mulholland 2000, Gooseff 2010).
45 Parameters such as flow velocities, residence times, and chemical concentrations vary within the
46 hyporheic zone and usually are intermediate between those in SW and GW (Hendricks and
47 White 1991, Hester and Doyle 2008). Hyporheic exchange is influenced by parameters such as
48 SW flow velocity, stage fluctuations, GW flow, and channel bedforms (Cardenas 2015, De Falco
49 et al. 2018, Hester et al. 2019). Hyporheic exchange through bedforms often dominates total
50 exchange relative to other morphologically driven exchange such as that due to meanders
51 (Gomez-Velez and Harvey 2014, Gomez-Velez et al. 2015) with multiple studies evaluating
52 dune-induced hyporheic hydraulics, transport, mixing, and reactions (Cardenas 2009, Bardini et
53 al. 2012, Hester et al. 2013, Zheng and Cardenas 2018, Singh et al. 2019).

54 Hyporheic zones are habitat for organisms such as microbes and macroinvertebrates.

55 Microorganisms can be classified based on their role in the trophic transfer of energy, for
56 example autotrophs, heterotrophic bacteria, protozoa, and fungi (Jones and Mulholland 2000).

57 Many studies focus on bacteria as they are the most abundant group in the hyporheic zone
58 (Findlay 2000). Prior field studies have measured microbial biomass or taxonomic composition
59 in river beds/banks and their controls such as sediment permeability, water chemistry, and
60 particulate organic matter (Nogaro et al. 2013, Stegen et al. 2016, Stegen et al. 2018). Yet these

61 studies did not resolve spatially explicit flowpaths, and thus could not evaluate effects of varying
62 transport or biogeochemical conditions on microbial metabolism or on spatial variability of
63 microbial activity and hence reaction rates. By contrast, laboratory studies of microbially-
64 mediated reactions in the hyporheic zone have been more spatially explicit. Some studies
65 measured microbially-mediated reactions and their effects in multiple dimensions, but measured
66 oxygenated area rather than microbial biomass (Kaufman et al. 2017, Galloway et al. 2019,
67 Wolke et al. 2020). Others directly measured microbial biomass and electron acceptor
68 consumption as affected by overall gaining or losing hydrologic conditions, the overlying water
69 column velocity, and sediment texture (De Falco et al. 2018, Cook et al. 2020). Yet lab studies
70 cannot conduct a full sensitivity analysis on potentially controlling hydraulic and biogeochemical
71 factors. Thus a key knowledge gap is how microbial growth and death processes, together with
72 varying availability of reactants, influence observed patterns of microbial abundance and
73 biogeochemical reactions in the hyporheic zone.

74 Modeling studies have explored controlling factors, but the vast majority did not explicitly
75 simulate microbial populations themselves (Kessler et al. 2013, Li et al. 2017a, Hester et al.
76 2018). These studies typically assumed rates of reaction are a function of maximum rates of
77 microbial utilization and concentrations of electron donors (i.e., organic carbon or ammonia
78 nitrogen) and electron acceptors (dissolved oxygen and nitrate) expressed using second-order
79 reactions. Implicit to this approach was a uniformly-distributed microbial population that
80 maintained steady biomass concentration over time independent of nutrient concentrations
81 (Zarnetske et al. 2012, Hester et al. 2014, Hester et al. 2019, Li et al. 2020, Sun et al. 2022). By
82 contrast, some modeling studies have simulated microbial populations, for example in seepage
83 from channels and effects of disconnection (Newcomer et al. 2016, Xian et al. 2019) or
84 hyporheic flow through bedforms and effects of heterogeneity and sediment transport (Caruso et
85 al. 2017, Ping et al. 2020, Ping et al. 2022). Such models that explicitly simulate growth and
86 decay of heterotrophic microbial populations consistently showed transient behavior in the
87 biomass concentration with the greatest increases expected at the influent boundary where
88 electron donors and acceptors are introduced (Molz et al. 1986, Widdowson et al. 1988, Caruso
89 et al. 2017, Ping et al. 2020). Nevertheless, a remaining knowledge gap is a systematic
90 exploration of the combined influence of key hydraulic and biogeochemical controls on
91 microbial populations and microbially-mediated reactions.

92 We simulated hyporheic zones induced by riverbed dunes, and compared aerobic microbial
93 metabolism dynamics when both accounting and not accounting for microbial growth and death
94 processes. We then conducted a sensitivity analysis of SW and GW boundary conditions. Our
95 objectives were to 1) simulate hyporheic aerobic microbial metabolism both with and without
96 microbial growth and death dynamics, 2) vary hydraulic and chemical boundary conditions, 3)
97 compare resulting variation in microbial biomass and spatial distribution, and 4) compare
98 resulting variation in DO and DOC mass and spatial distribution. We hypothesize that allowing
99 microbial populations to grow and die in response to temporally and spatially varying reactant
100 concentrations within the hyporheic zone will allow the microbes to consume more reactants
101 with smaller microbial populations, thereby increasing the efficiency of microbial consumption.
102 We further hypothesize that hydraulic controls on hyporheic flow and hence hyporheic flowpaths
103 and residence times will exert an important control on reactant concentrations and hence
104 microbial populations.

105

106 **2. Methods**

107 We simulated hyporheic flow through riverbed dunes constrained by background upwelling
108 groundwater (GW), transport of dissolved oxygen (DO) and dissolved organic carbon (DOC)
109 from the overlying water column into the hyporheic zone, and growth and death of an attached
110 aerobic microbial population within the submerged pore space including their microbially-
111 mediated metabolism of DOC and DO.

112 **2.1 Model Codes and Governing Equations**

113 The core of the numerical experiments were conducted using (1) MODFLOW (Harbaugh 2005)
114 to model GW hydraulics, and (2) SEAM3D (Waddill and Widdowson 1998, 2000) to model DO
115 and DOC transport, microbial aerobic respiration, and microbial growth and death. In addition,
116 we used OpenFOAM (Weller et al. 1998) to provide the spatially varying pressure along the top
117 surface of the dune (needed in MODFLOW) by solving the steady-state Reynolds Averaged
118 Navier Stokes (RANS) equations for the overlying river water for a range of conditions.

119 We used MODFLOW (Harbaugh 2005) to model GW hydraulics in two dimensions
120 (longitudinally along channel, and vertical). MODFLOW uses a control-volume finite-difference
121 method (CVFD) to solve the GW flow equation,

$$\frac{\partial}{\partial x_i} \left(K_i \frac{\partial h}{\partial x_i} \right) + Q'_s = SS \frac{\partial h}{\partial t} \quad (1)$$

122 where x_i (L) indicates distance along the i^{th} Cartesian axis (in this case x and z), K_i (L/T) is
 123 hydraulic conductivity in the i^{th} direction; h is hydraulic head (L); Q'_s is volumetric
 124 inflow/outflow per unit volume into the system (T^{-1}); SS is specific storage of the matrix (L^{-1});
 125 and t is time (T). MODFLOW was used in steady state mode, setting the transient term of
 126 equation (1) to zero. We used MODPATH (Pollock 2012) to track particles and calculate
 127 residence times for each upper and lower boundary cell. Use of OpenFOAM for the SW head
 128 boundary condition is discussed in Section 2.3.

129 Electron acceptor (DO) and organic carbon substrate (labile fraction of DOC) transport,
 130 microbial aerobic respiration, and microbial growth and death were modeled with SEAM3D
 131 (Waddill and Widdowson 1998, 2000). SEAM3D solves the advection, dispersion, and chemical
 132 reaction equation in a GW system,

$$\frac{\partial(\theta C^k)}{\partial t} = \frac{\partial}{\partial x_i} \left(\theta D_{ij} \frac{\partial C^k}{\partial x_j} \right) - \frac{\partial}{\partial x_i} (\theta v_i C^k) + Q'_s C_s^k + R \quad (2)$$

133 where C^k is the dissolved concentration (ML^{-3}) of species k (in this case DO and DOC); θ is the
 134 effective porosity of the medium (dimensionless); D_{ij} is the hydrodynamic dispersion coefficient
 135 tensor (L^2T^{-1}), v_i is porewater velocity (LT^{-1}); C_s^k is the concentration of any given source or sink
 136 for a species k (ML^{-3}); and R ($ML^{-3}T^{-1}$) is the chemical reaction term. In this study, R is a
 137 biodegradation sink term for aerobic microbial metabolism given by Equations 3A and 3B for
 138 DOC and DO, respectively

$$R_{DOC} = - \left(\frac{M_b}{\theta} \right) v^{max} \left(\frac{C^{DOC}}{K^{DOC} + C^{DOC}} \right) \left(\frac{C^{DO}}{K^{DO} + C^{DO}} \right) \quad (3A)$$

$$R_{DO} = - \left(\frac{M_b}{\theta} \right) \gamma v^{max} \left(\frac{C^{DOC}}{K^{DOC} + C^{DOC}} \right) \left(\frac{C^{DO}}{K^{DO} + C^{DO}} \right) \quad (3B)$$

139 where M_b is the aerobic microbial biomass concentration (ML^{-3}); C^{DOC} and C^{DO} are the
 140 concentrations of DOC and DO (ML^{-3}), respectively; v^{max} is the maximum specific rate of
 141 utilization (T^{-1}); γ is the DO use coefficient for aerobic metabolism (M/M); and K^{DOC} and K^{DO}

142 are the half saturation constants for DOC and DO (ML^{-3}), respectively (Molz et al. 1986,
143 Widdowson et al. 1988).

144 Microbial mass balance for the growth and death of the aerobic population enabled simulation of
145 the temporal changes in the spatial distribution of microbial biomass concentration (Waddill and
146 Widdowson 1998),

$$\frac{1}{M_b} \frac{dM_b}{dt} = -k_d + G_b \quad (4)$$

147 where k_d is the effective death rate (T^{-1}) and G_b is the growth rate of the aerobic population due
148 to available DOC and DO (T^{-1}). Growth rate is a function of the specific substrate utilization rate
149 v^{max} (T^{-1}), in this case for aerobic metabolism as given by

$$G_b = Yv^{max} \left(\frac{C^{DOC}}{K^{DOC} + C^{DOC}} \right) \left(\frac{C^{DO}}{K^{DO} + C^{DO}} \right) \quad (5)$$

150 where Y is the biomass yield coefficient (MM^{-1}). The effective death rate is given by

$$k_d = \max[0, k_d^{bk} - (G_b^{bk} + G_b)] \quad (6)$$

151

152 where the subscript “bk” signifies background (initial) growth and death rates. The model
153 calculates the background growth rate based on the initial electron acceptor concentrations using

$$G_b^{bk} = Yv^{max} \left(\frac{C^{DO}}{K^{DO} + C^{DO}} \right) \quad (7)$$

154

155 The background effective death rate (k_d^{bk}) is set equal to the background growth rate to simulate
156 steady-state initial conditions when the microbial growth and decay are in balance throughout the
157 system at time zero. We did not simulate other microbial populations besides strict aerobes (e.g.,
158 facultative microbes) for this study.

159 Given our relatively oligotrophic conditions (DOC 1-15 mg/L, Table 1 and Section 2.3),
160 we simplified our model to not include the effects of microbial growth on porosity and therefore
161 hydraulic conductivity and porewater flow. This is consistent with field, laboratory, and
162 numerical studies of microbial growth in hyporheic and aquatic sediments where DOC levels

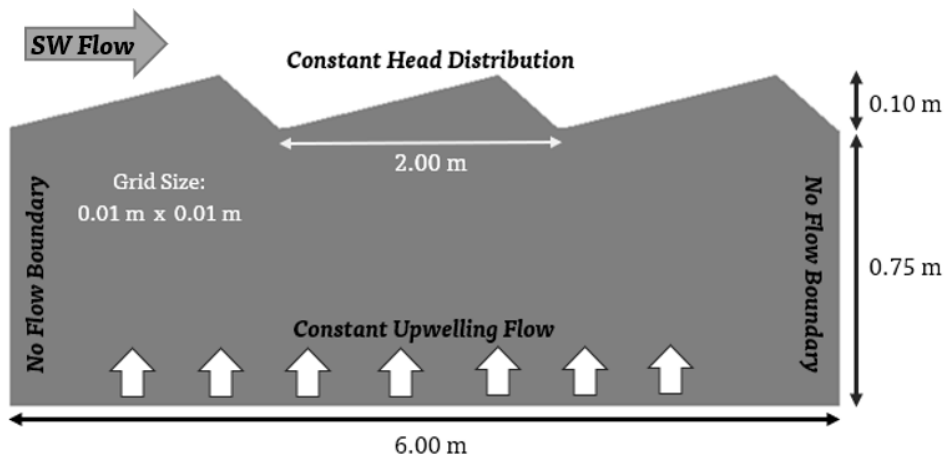
163 were low (< 20 mg/L), where available substrate was insufficient to cause bioclogging (Nogaro
164 et al. 2013, Mendoza-Lera et al. 2017, De Falco et al. 2018, Ping et al. 2020, Xian et al. 2023),
165 and thus hydraulic conductivity was the main controlling factor (Mendoza-Lera et al. 2019). We
166 similarly assumed that the contribution of microbial death to the labile DOC supply was
167 negligible.

168

169 **2.2 Model Domain and Grid**

170 We first tested models with one dune, three dunes and five dunes to evaluate the effect on the
171 central dune of treating upstream and downstream groundwater boundaries as no-flow
172 boundaries. The central dune in the three-dune model (Figure 1) showed differences of up to 5%
173 in total microbial mass, DO and DOC when compared to the one-dune model. Additionally,
174 more than half of the domain showed differences larger than 1% when compared to the one-dune
175 model. However, the differences between the five-dune model and the three-dune model were
176 negligible as the total microbial mass, DO and DOC differed by approximately 0.01%
177 (Supporting Information 1). This suggested that there was no need to increase the number of
178 dunes beyond three and that using results from the central dune of a three-dune model was the
179 optimal choice in terms of results that were not influenced by the no-flow boundary conditions
180 while also reducing computational time.

181 All modeled dunes had a length of 2 meters and a height of 10 centimeters, or a dune length to
182 height ratio of 20, which is broadly consistent with field and laboratory dune geometry scaling at
183 bedload-dominated transport stages in creeks and shallow rivers (Best and Kostaschuk 2002,
184 Bradley and Venditti 2019, Cisneros et al. 2020). Grid cell size was set to 1 cm by 1 cm, and
185 model depth was set to 0.75 m for a total of 0.85 m at the peak of the dune, resulting in a total of
186 48,677 grid cells.



187

188 *Figure 1. MODFLOW and SEAM3D model domain*

189

190 **2.3 Model Parameters and Boundary Conditions for Base Case and Sensitivity Analysis**

191 We performed a sensitivity analysis that varied hydraulic and DO/DOC concentration boundary
 192 conditions one at a time relative to a base case (Table 1). This section provides details on model
 193 parameters and their justification.

194 Table 1. Model Parameters and Boundary Conditions for Base Case and Sensitivity Analysis

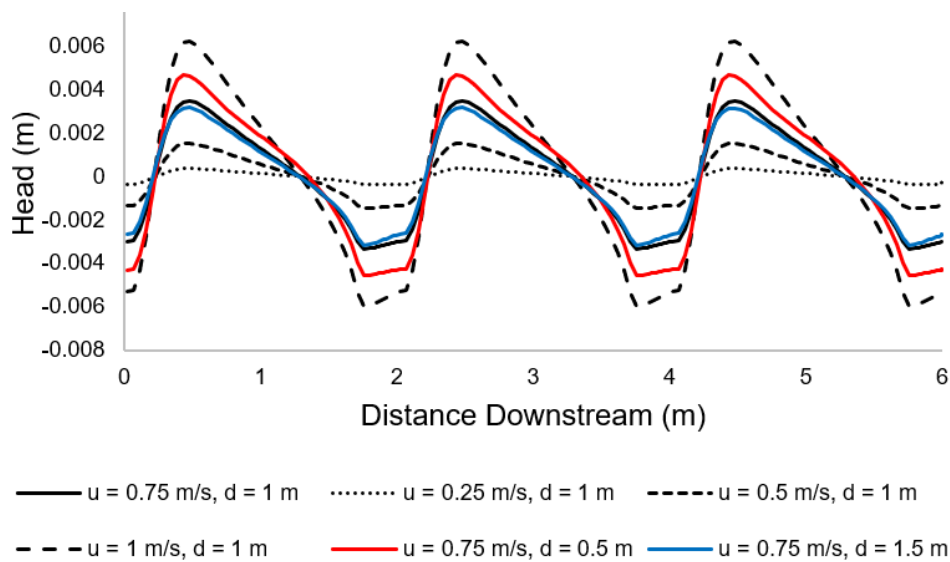
Parameter	Abbreviation	Base Case Value	Range Varied in Sensitivity Analysis	Units	
Varied in Sensitivity Analysis					
MODFLOW/ OpenFOAM	Bottom (GW) boundary upwelling flux	Bottom q	760	76 – 2,600	m ³ /d
	Overlying water column (SW) depth in OpenFOAM	d*	1	0.5 – 1.5	m
	Overlying water column depth-averaged (SW) velocity on OpenFOAM	u*	0.75	0.25 - 1	m/s
SEAM3D	Top boundary (SW) DO concentration	SW DO	5	1 – 15	mg/L
	Top boundary (SW) DOC concentration	SW DOC	5	1 – 15	mg/L
Constants					
MOD- FLOW	Hydraulic conductivity	K	100	-	m/d
	Horizontal to vertical anisotropy	A	1:1	-	
SEAM3D	Longitudinal dispersivity	α_L	0.01	-	m
	Transverse dispersivity	α_T	0.001	-	m
	Biomass yield coefficient	Y	0.25	-	g/g
	Effective porosity	θ	0.3	-	-
	Max specific rate of DOC utilization	v^{max}	23.64	-	g/g/d
	DO use coefficient	γ	1.07	-	g/g
	DOC half saturation constant	K^{DOC}	8.68	-	g/m ³
DO half saturation constant	K^{DO}	5.28	-	g/m ³	

195 SW= surface water, GW = groundwater

196 *varied in OpenFOAM to create top (SW) hydraulic head boundary conditions for MODFLOW.

197 2.3.1 MODFLOW Boundary Conditions and Parameters

198 The cells of the top (SW) boundary (Figure 1) were assigned a spatially-varying distribution of
199 constant heads from steady-state computational fluid dynamics (CFD) water column simulations
200 of the overlying river using OpenFOAM (Weller et al. 1998) (Figure 2). OpenFOAM solved the
201 Reynolds-averaged Navier-Stokes (RANS) equations using the $k - \Omega$ turbulence closure
202 scheme. SW depth (d , L) and depth-averaged SW downstream velocity (u , LT^{-1}) were varied in
203 OpenFOAM to generate different top boundary conditions for MODFLOW (Table 1, Figure 2).
204 These ranges of u and d represent SW hydraulic conditions where dunes would form (Colombini
205 and Stocchino 2008) and migrate downstream. Such depth-averaged water column velocities
206 (i.e., 0.25 - 1 m/s) are well within the range of expected river water velocities for the presence of
207 dunes in rivers. Values of u higher than 1.0 m/s would cause dunes to erode and disappear,
208 given the SW depths (d) and dune configuration used in the simulations. Values of u lower than
209 0.25 m/s would create situations where the SW flow does not have enough strength to create the
210 dunes in the first place. The resulting overall pattern of head distribution at the sediment-water
211 interface (Figure 2) is consistent with the laboratory measurements by Fehlman (1985).
212 Additional details of the OpenFOAM simulations, including benchmarking against prior
213 laboratory and modeling studies, are given in Lotts (2022).



215 *Figure 2. Top (surface water, SW) boundary hydraulic head distributions generated with*
216 *OpenFOAM for the surfaces of the three dunes in the model domain (u = depth-averaged*
217 *velocity in overlying SW, d = average depth in overlying SW).*

218

219 Each cell of the bottom boundary was assigned constant flow representing the upward GW
220 discharge into SW (Cardenas and Wilson 2006, 2007, Hester et al. 2013). GW upwelling flow
221 (q) for the base case was set so that the lowest point of the hyporheic flow cell in the vertical
222 direction was close to the midpoint of the model domain; this corresponded to 760 m³/d. The
223 upper limit for the upwelling flow (0.03 m³/s) caused the hyporheic flow cell to almost disappear
224 and the lower limit (76 m³/d) caused it to almost meet the bottom of the domain. The sides of the
225 domain were treated as no flow boundaries. The base case model had a homogeneous hydraulic
226 conductivity (K) of 100 m/d, similar to previous studies of hyporheic flow in dunes (Cardenas
227 and Wilson 2007, Hester et al. 2013).

228

229 *2.3.2. SEAM3D Boundary and Initial Conditions and Parameters*

230 Top (SW) DO and DOC boundary concentrations (C^{DO} and C^{DOC} , respectively) in SEAM3D
231 were set as uniform along the dune surface and constant in time. For the base case, both
232 concentrations were set to 5 mg/L, which are intermediate within the ranges used previously in
233 hyporheic zone sensitivity analysis (Bardini et al. 2012, Hester et al. 2014) and stream water
234 quality (Dubrovsky et al. 2010, Corsi et al. 2011) studies. These values also correspond to a
235 DO:DOC ratio of 1:1, which is similar to the DO use coefficient γ of 1.07.

236 For the sensitivity analysis, DO top boundary concentration was varied from 1 mg/L to 15 mg/L
237 in accordance with the ranges in the literature (Dubrovsky et al. 2010, Corsi et al. 2011, He et al.
238 2011, Bardini et al. 2012, Rajwa-Kuligiewicz et al. 2015) and to cover the full range of DO
239 saturation (14.6 to 7.6 mg/L at 0 °C to 30 °C, respectively). DOC was also varied from 1 mg/L
240 to 15 mg/L, again within the ranges observed in prior studies (Hester et al. 2014, Lee et al.
241 2016), and consistent with oligotrophic conditions (Nogaro et al. 2013, De Falco et al. 2018,
242 Ping et al. 2020, Xian et al. 2023).

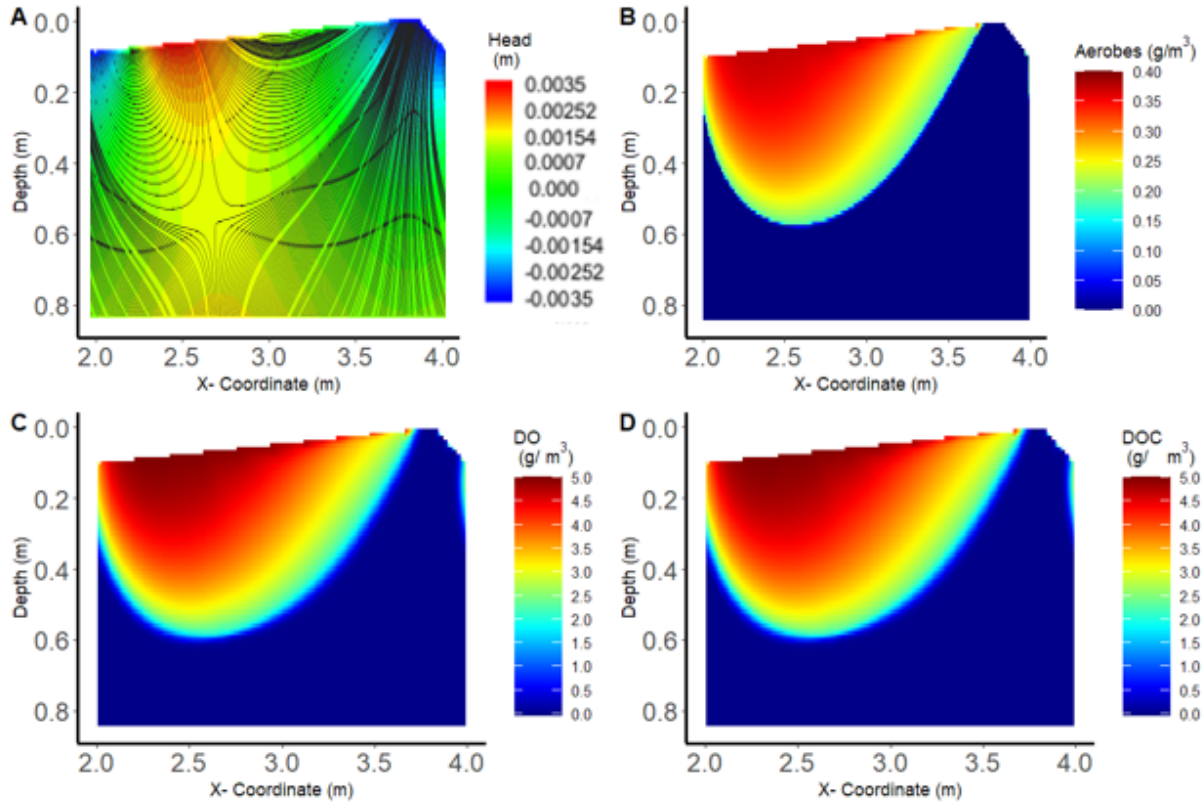
243 The initial concentrations for DO, DOC, and biomass (C^{DO} , C^{DOC} , and M_b , respectively) were set
244 as spatially uniform throughout the model domain. The base case was simulated multiple times
245 with different initial conditions up to a total simulation time of 10 days to achieve a steady state
246 condition. Varying the initial conditions while keeping top boundary DO and DOC constant did
247 not much influence the final steady state total biomass (Supporting Information 1), which is the
248 focus of our reported results (Section 3). Thus the DO and DOC initial concentration was set
249 arbitrarily to 4 mg/L, similar to top boundary concentrations but slightly lower, consistent with
250 Bardini et al. (2012) and Hester et al. (2014). Initial biomass was set as uniform at 0.125 g/m³
251 such that the total initial biomass in the model domain was almost the same as the base case
252 steady state total biomass. This value is also arbitrary, but consistent with prior studies (Xian et
253 al. 2019, Ping et al. 2020, Ping et al. 2022). The maximum specific substrate utilization rate
254 (v^{max}) and the biomass yield coefficient (Y) were (Table 1) based on previous modeling studies
255 (Essaid et al. 1995, Hester et al. 2014).

256

257 **3. Results**

258 **3.1 Base Case**

259 MODFLOW hydraulic results indicate water entered the domain in the higher pressure zone in
260 the middle of the upstream (stoss) side of the dune and left at the lower pressure zone centered
261 on the lee side (Figure 3A) consistent with prior studies (Elliott and Brooks 1997, Cardenas and
262 Wilson 2006, Hester et al. 2013). Flow paths indicate a hyporheic flow cell with residence times
263 that ranged from 0 to 60 hours. Steady-state SEAM3D results for the growth/death base case
264 show that DO, DOC, and aerobic microbial biomass were concentrated within the hyporheic
265 flow cell, with higher concentrations wherever water entered the system and lower where water
266 left the system (Figure 3B, C, D). Concentrations were roughly inversely correlated with distance
267 to the edge of the hyporheic flow cell, and thus subsurface residence time.



268

269

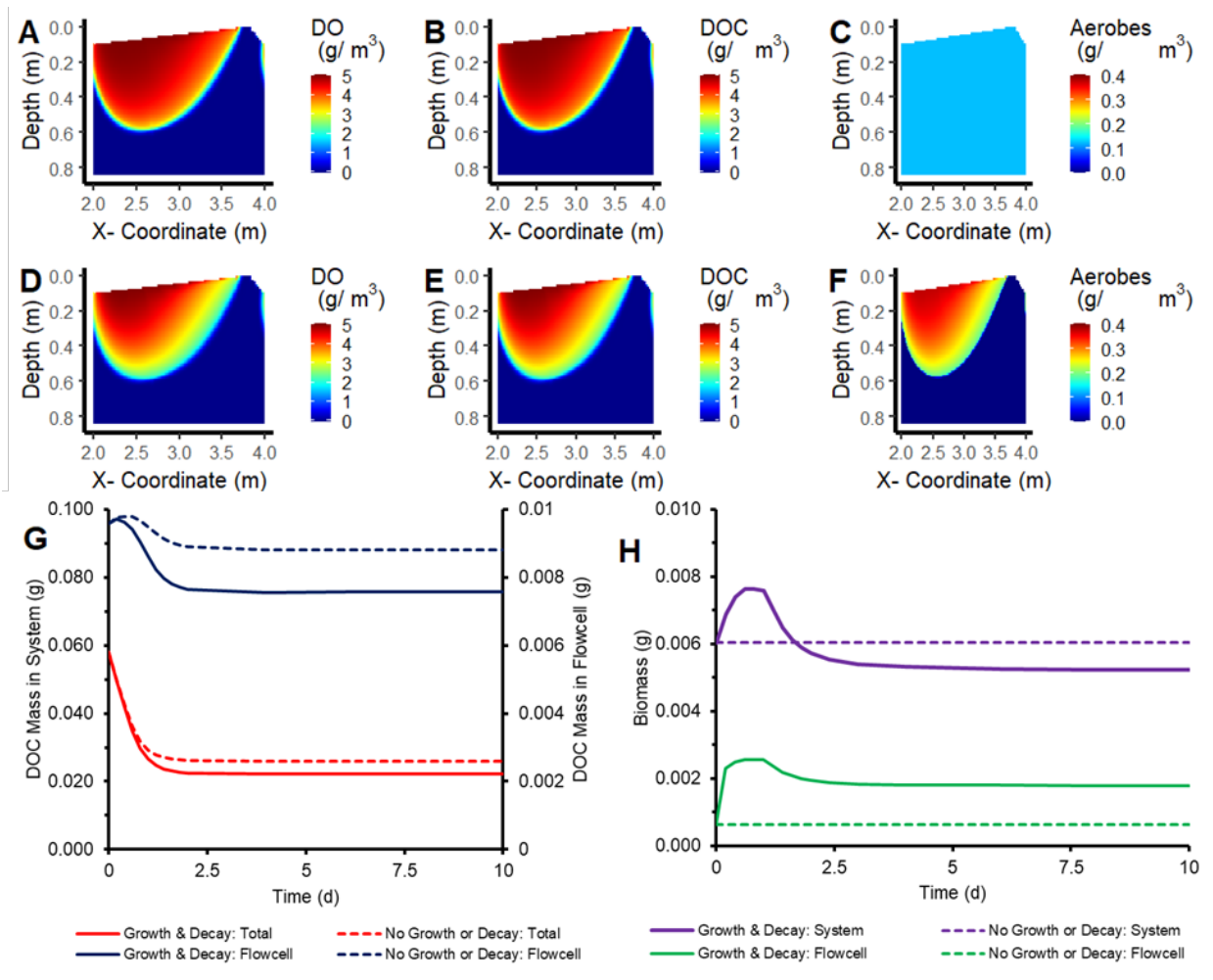
270 *Figure 3. Spatial distribution of A) hydraulic head and flowpaths, B) aerobic microbial biomass,*
 271 *C) dissolved oxygen (DO), and D) dissolved organic carbon (DOC) for the growth/death base*
 272 *case simulation. All results are steady-state which for SEAM3D are output at a simulation time*
 273 *of 10 days. Results presented are for central dune from the three-dune model domain (Figure 1).*

274

275 When microbial growth/death were not simulated, our SEAM3D results were similar to those in
 276 Hester et al. (2013) with the formation of a thin steady-state GW-SW water mixing zone (Figure
 277 4A, B) and a uniform spatial distribution of aerobes (Figure 4C). By contrast, growth/death
 278 dynamics caused a broader area of intermediate DO and DOC concentrations (i.e. a lower
 279 concentration gradient) (Figure 4D, E), consistent with the spatial distribution of aerobes
 280 concentrated where the DO and DOC were present (Figure 4F). Biomass in the no-growth/no-
 281 death scenario remained unchanged with time as expected, while that for the growth/death
 282 scenario stabilized by about 3 days in both the hyporheic flowcell and the larger model domain

283 (Figure 4H). By contrast, steady state DOC concentrations were reached much sooner (Figure
284 4G), after approximately one day of simulation. The DO concentrations (not shown) followed an
285 identical pattern and difference in magnitude as the DOC concentrations.

286 There was 12% lower overall steady-state microbial biomass within the model domain for the
287 growth/death scenario (6.0 mg, Figure 4F, H) than for the no growth/no death scenario (5.2 mg,
288 Figure 4C, H). In contrast, the steady-state microbial biomass within the hyporheic flowcell for
289 the growth/death scenario (1.8 mg, Figure 4H) was greater by a factor of 3.0 compared to the
290 steady-state biomass for the no growth/no death scenario (0.6 mg, Figure 4H). While the fact that
291 growth/death provides greater biomass in the hyporheic flowcell and lower biomass in the total
292 model domain is a robust finding, we note that the magnitude of this difference is arbitrary based
293 on model domain size because the die-out of microbes at the bottom of the growth/death model
294 domain means that increasing the depth of the model domain would increase the microbial mass
295 in the no growth/no death scenario relative to the growth/death scenario (i.e. the differences
296 would increase). There was 14% lower steady-state DOC mass in the both the model domain
297 and the hyporheic flowcell for the growth/death scenario (22.3 and 7.6 mg, respectively) than in
298 the no growth/no death scenario (25.9 and 8.8 mg, respectively) (Figure 4G), and in contrast to
299 biomass, this finding is not arbitrary as additional model depth at zero concentration does not
300 affect total solute mass present. Finally, the steady-state rate of total DOC consumption
301 throughout the model domain was 85% for the growth than no-growth scenarios (not shown). In
302 sum, at steady-state, the growth scenario showed greater DOC consumption due to more biomass
303 in the hyporheic flowcell, resulting in less DOC remaining in the model domain.



304

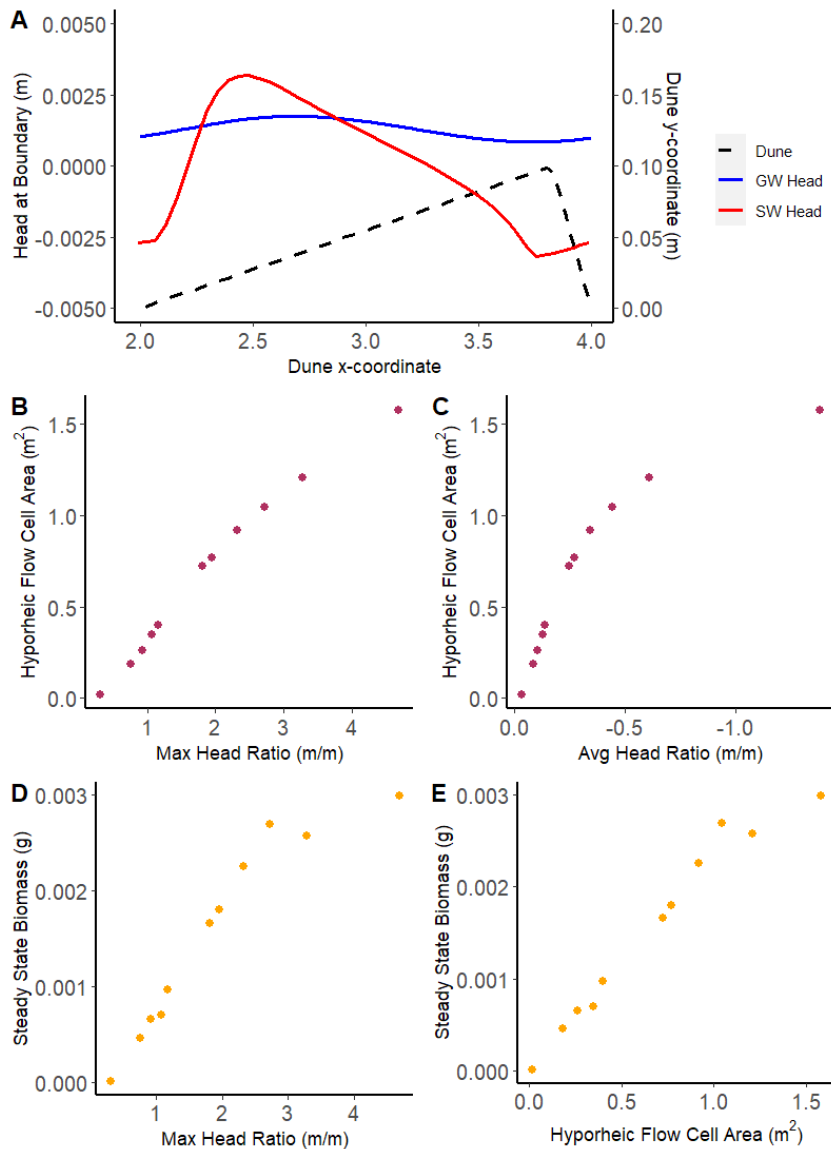
305 *Figure 4. A) Dissolved oxygen (DO) spatial distribution, B) dissolved organic carbon (DOC)*
 306 *spatial distribution, and C) aerobic microbial biomass spatial distribution for no growth/no*
 307 *death conditions. D) DO spatial distribution, E) DOC spatial distribution, and F) aerobic*
 308 *microbial biomass spatial distribution for growth/death conditions. G) Total mass of DOC in*
 309 *model domain and the hyporheic flowcell for both base cases (growth/death and no growth/no*
 310 *death). H) Total biomass in model domain and the hyporheic flowcell for both base cases*
 311 *(growth/death and no growth/no death). Results presented in panels A-F are for central dune*
 312 *from the three-dune model domain at steady-state ($t=10$ days).*

313

314 3.2 Hydraulic Sensitivity Analysis

315 In our sensitivity analysis of hydraulic parameters in MODFLOW, we varied top boundary
 316 surface water (SW) depth and depth-averaged velocity (via OpenFOAM) and bottom boundary

317 groundwater (GW) upwelling flow (Table 1). Together these parameters determine the
 318 hydraulic head distributions at the top (SW) and bottom (deeper GW) boundaries of the model
 319 domain, respectively. Model results indicate that both boundary heads exhibited non-uniform
 320 spatial distributions (Figures 2, 5A). To simplify our analysis of controlling factors, we present
 321 the results using the ratios of both the maximum and average SW heads to maximum GW head,
 322 rather than the actual heads, because the relative balance of these two heads is a key control on
 323 hyporheic flow cell size or area (Hester and Doyle 2008) (Figure 5A).



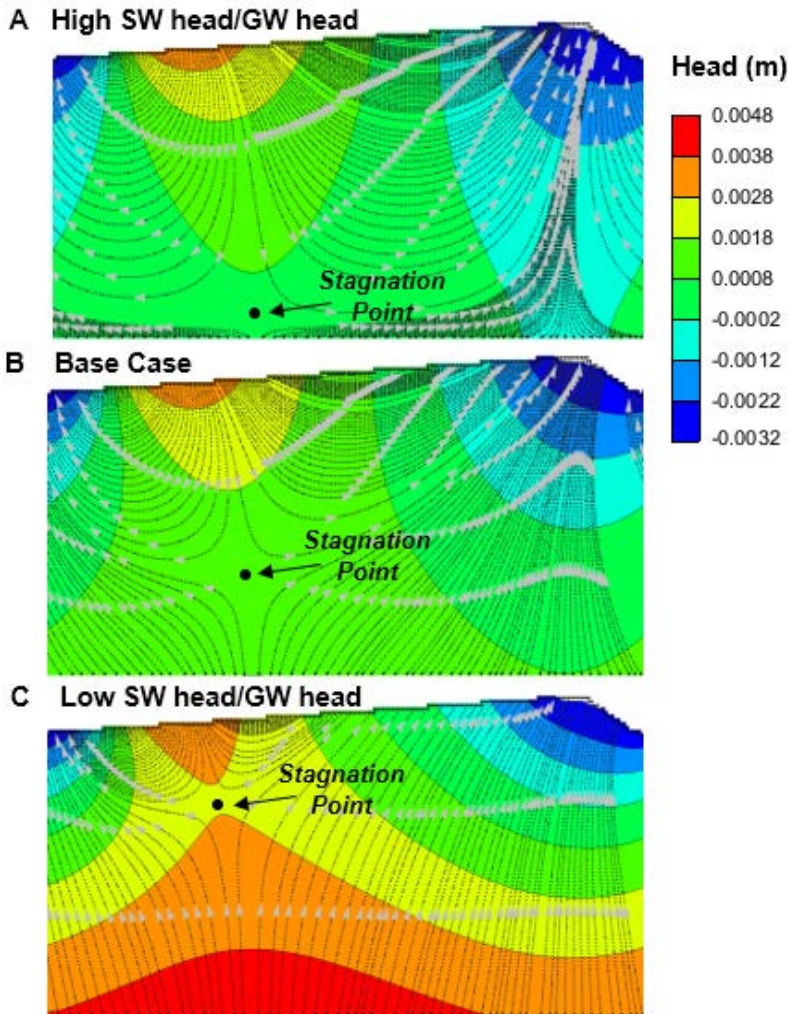
324

325 *Figure 5. A) Surface water (SW) and groundwater (GW) head distributions along the top and*
 326 *bottom boundaries of the central dune of the model for base case scenario, B) Steady state*

327 *hyporheic flow cell area as a function of maximum SW to maximum GW head ratio, C) Steady*
328 *state hyporheic flow cell area as a function of average SW to average GW head ratio, D) Steady*
329 *state biomass (with growth/death) vs maximum head ratio, E) Steady state biomass (with*
330 *growth/death) vs hyporheic flow cell area. Results presented are steady state ($t= 10$ days) for*
331 *central dune from the three-dune model domain (Figure 1). We approximated flow cell area in*
332 *C and D as including all cells with DO concentration > 0.1 mg/L (this matched the flow paths*
333 *corresponding to the hyporheic flow cell, Supporting Information 2).*

334

335 As SW/GW head ratio decreased, the size or area of the hyporheic flow cell induced by the dune
336 decreased (Figure 5B). The area of this cell increased almost linearly with max boundary head
337 ratio but levelled off slightly at higher ratios, whereas area leveled off more significantly above
338 average ratios of approximately -0.4 m/m (Figure 5B, C). The levelling off in both curves could
339 indicate growth being limited by adjacent dunes. For example, even if hyporheic cell width and
340 depth are both linearly correlated to average head ratio, as width or depth are in turn limited by
341 other factors such as the existence of adjacent dunes, hyporheic cell growth becomes non-linear.
342 In Figure 6A, for instance, the hyporheic flow cell is limited by the bottom boundary of the
343 domain and the flow paths from adjacent dunes due to the high SW/GW head ratio (3.28 m/m),
344 which is not observed in the base case (Figure 6B, SW/GW head = 1.96 m/m) or the low
345 SW/GW head ratio (Figure 6C, SW/GW head = 1.16 m/m).



346

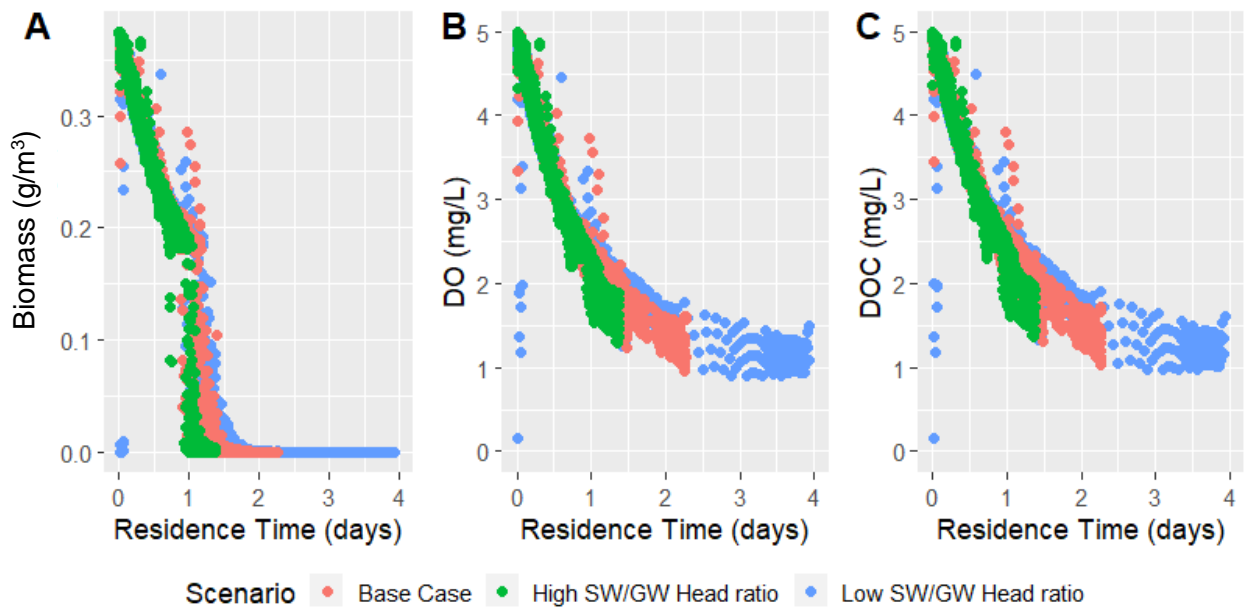
347 *Figure 6. Head distributions and flow paths for example hydraulic conditions, including A)*
 348 *surface water head/groundwater head ratio (SW/GW) higher than base case (SW/GW = 3.28*
 349 *m/m; $d = 1$ m; $u = 0.75$ m/s, GW inflow = 259 m³/d), Base case (SW/GW = 1.96 m/m; $d = 1$ m;*
 350 *$u = 0.75$ m/s, GW inflow = 760 m³/d), and C) SW/GW lower than base case (SW/GW = 1.16*
 351 *m/m; $d = 1$ m; $u = 0.75$ m/s, GW inflow = 1560 m³/d). Results presented are steady state for*
 352 *central dune from the three-dune model domain (Figure 1).*

353

354 SEAM3D results overall indicate that aerobic microbial biomass increased with maximum SW
 355 head/GW head ratio (Figure 5D) and hyporheic flow cell area (Figure 5E). This makes sense
 356 because the area of suitable habitat simultaneously increased. However, there is some scatter,

357 particularly at larger flow cell areas, because head ratio does not account for effect of residence
358 time. In other words, even if two different hydraulic conditions happened to have the same
359 maximum SW head/GW head ratio (no two model scenarios we ran represent exactly this
360 situation), their residence time distributions may differ and thus, the availability of DO and DOC
361 in the dune due to upstream reactions.

362 The results showed a decrease in biomass with increasing GW residence time within the dune
363 (Figure 7). This makes sense as both DO and DOC have more opportunity to have been
364 consumed, and lowered DO/DOC concentrations would lead to decreased aerobic microbial
365 biomass, as time spent in the subsurface increased. Biomass and DO/DOC concentrations always
366 decreased nonlinearly with residence time, with lower slopes at higher residence times. For
367 residence times greater than 1 day, biomass plummeted to a concentration of almost 0 mg/L
368 (Figure 7A).



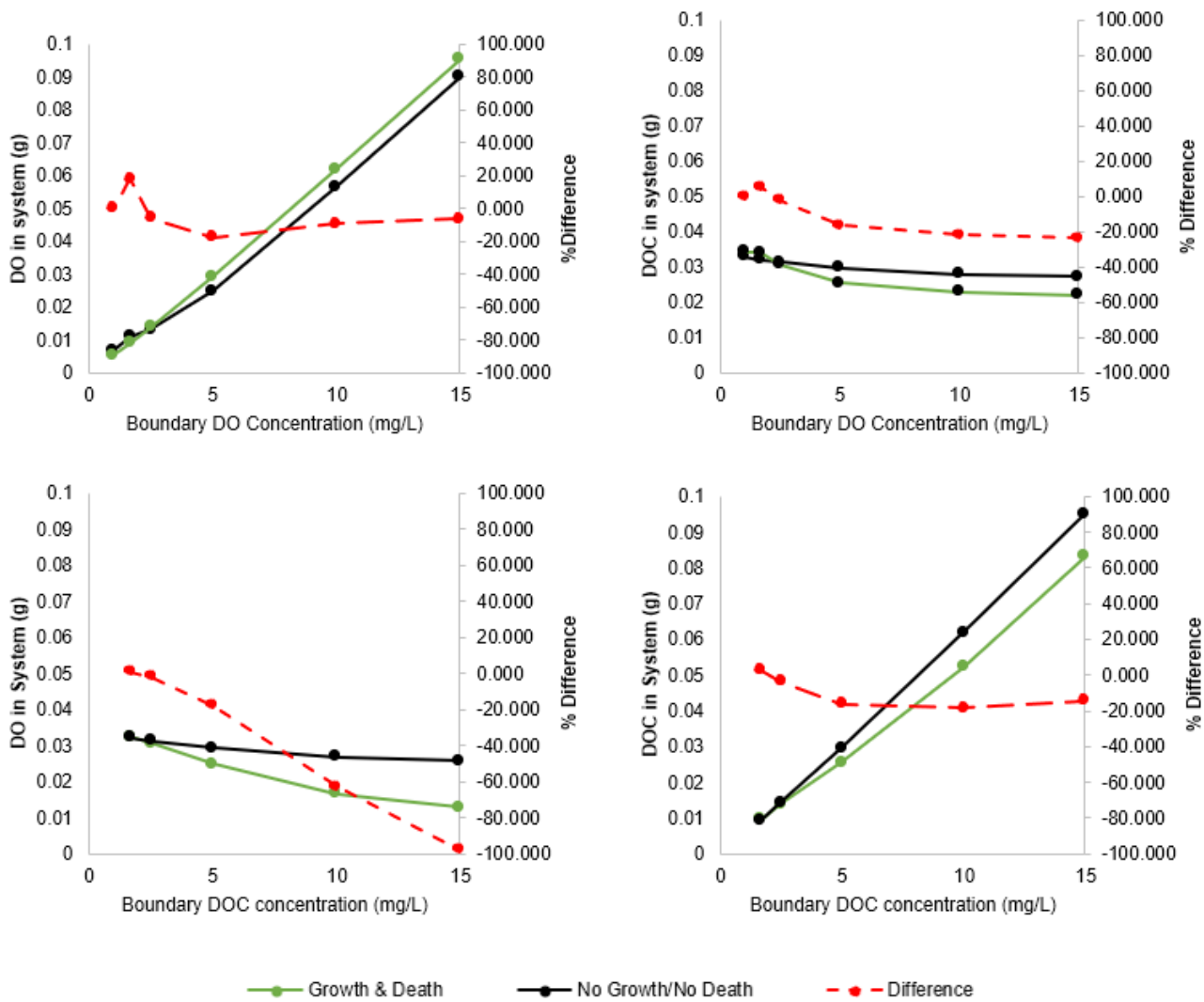
369
370 *Figure 6. Aerobic microbial biomass concentration, dissolved oxygen (DO) concentration, and*
371 *dissolved organic carbon (DOC) concentration vs. residence time for every cell in the model*
372 *domain for selected hydraulic sensitivity analysis model runs, including base case (surface water*
373 *groundwater head ratio (SW/GW) = 1.96 m/m; Figure 6b), high SW/GW (= 3.28 m/m; Figure*
374 *6a), and low SW/GW (= 1.16 m/m, Figure 6c). Residence times calculated using MODPATH.*
375 *Results presented are for central dune from the three-dune model domain (Figure 1).*

376

377 **3.3 Oxygen and Organic Carbon Sensitivity Analysis**

378 *3.3.1 Steady State Results*

379 In our sensitivity analysis of DO and DOC in SEAM3D, we varied top (SW) boundary
380 concentrations (Table 1) to see their effect on aerobic microbial biomass, GW DO, and GW
381 DOC. All simulations reached steady state for DO, DOC, and microbial biomass within about 2
382 days model time. As expected, total DO and DOC mass within the central dune increased almost
383 linearly with top boundary DO and DOC, respectively (Figure 8A, D) and did not increase
384 otherwise (Figure 8B, C). Additionally, trends in DO and DOC concentrations within the
385 hyporheic zone were roughly the same for the growth/death and no growth/no death models. In
386 general, total DO and DOC masses in the dune were lower for the growth/death model than the
387 no growth/no death model, and the absolute difference (units of mass) between the growth/death
388 and no growth/no death models became larger with increasing top boundary concentrations of
389 DO and DOC (Figure 8, left y-axes). Absolute (mass) differences were also greater for boundary
390 DOC (Figure 8C, D) than boundary DO (Figure 8A, B). On the other hand, percent differences
391 (Figure 8, right axes) generally did not show monotonic patterns (with the exception of panel C)
392 and were mostly below 25%.



393

394 *Figure 8. Total chemical mass for base case hydraulic conditions as a function of top (surface*
 395 *water, SW) boundary conditions, including A) dissolved oxygen (DO) in dune vs boundary DO*
 396 *concentration, B) DO in dune vs boundary dissolved organic carbon (DOC) concentration, C)*
 397 *DOC in dune vs boundary DO concentration, D) DOC in dune vs boundary DOC concentration.*
 398 *Right y-axes shows percent difference between the growth/death results and the no growth/no*
 399 *death results. Results presented are steady state at $t = 10$ days for central dune from the three-*
 400 *dune model domain (Figure 1).*

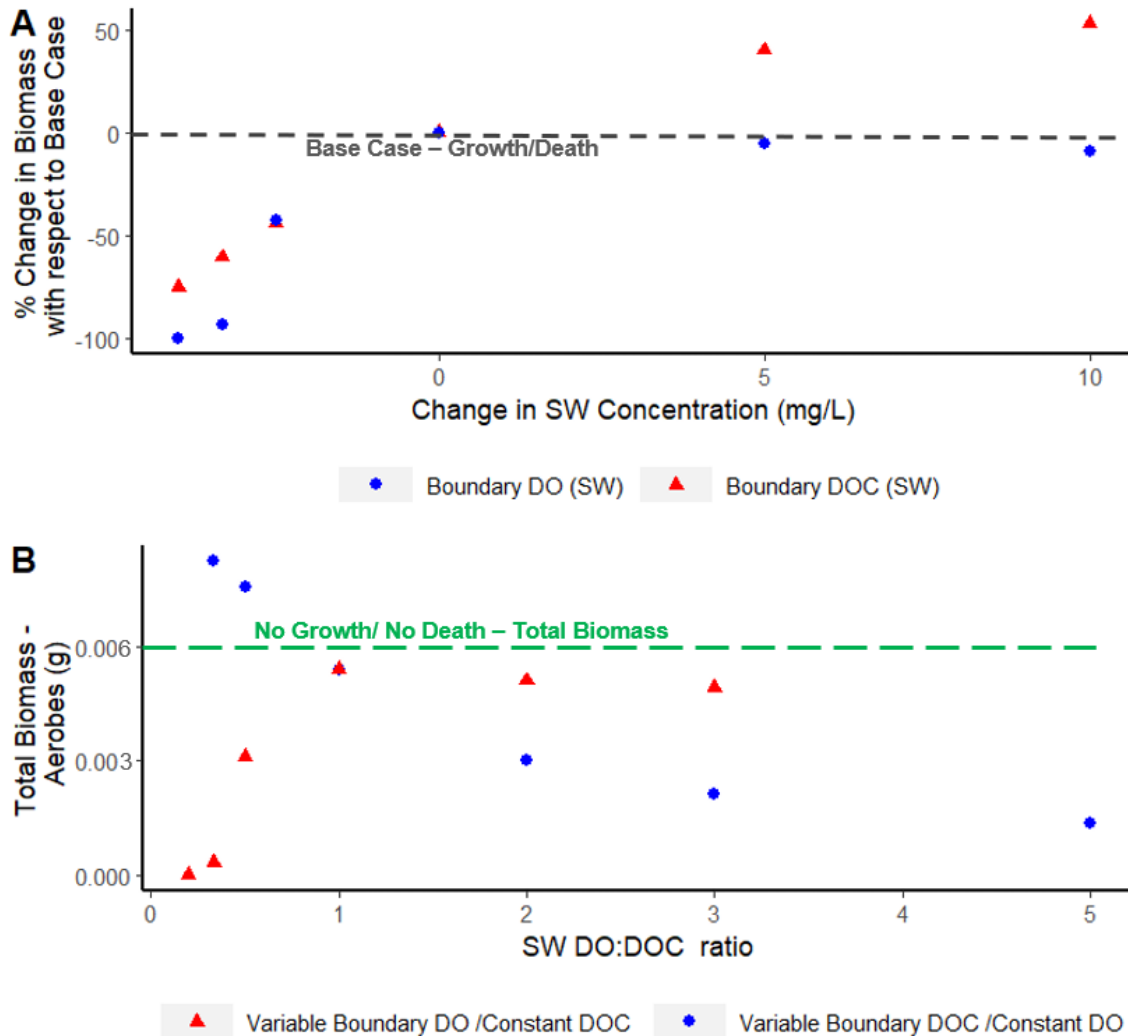
401

402 An increase in top boundary DOC concentration above that in the base case led to increased total
 403 microbial biomass within the central dune, while increasing DO caused a small (< 10%) decrease

404 in total biomass (Figure 9A). On the other hand, decreasing both DO and DOC below those of
405 the base case caused microbial mass to decrease, and the effect was more dramatic for DO which
406 dropped by up to ~100%. This indicates that both DO and DOC limit microbial growth but DO
407 restricts growth more at lower concentrations.

408 These biomass trends can be replotted as a function of the SW DO:DOC ratio (Figure 9B). For
409 all model scenarios where SW DOC was held constant, a high DO:DOC ratio implies that SW
410 DO was higher than the condition used in the base case; by contrast, for all scenarios where SW
411 DO was held constant, a high ratio implies that SW DOC was lower than that of the base case.
412 For example, a ratio of 3 could either represent a DO:DOC ratio of 15:5 (more DO than base
413 case) or 5:1.67 (less DOC than base case). This ratio is helpful to compare different model runs,
414 as a ratio of 0.5 for constant SW DO (5:10 – red triangles in Figure 9B) would be comparable to
415 a ratio of 2 for constant SW DOC (10:5 – blue squares in Figure 9B). When varying SW DO (red
416 triangles on Figure 9B), biomass maxed out at a ratio of ~1:1, this could be related to the DO use
417 coefficient γ of 1.07.

418



420

421 *Figure 9. A) Percent changes in total aerobic microbial biomass vs change from base case of top*
 422 *(surface water, SW) boundary concentrations of dissolved oxygen (DO) or dissolved organic*
 423 *carbon (DOC), B) Total aerobic microbial biomass in central dune vs top boundary DO:DOC*
 424 *ratio where ratio is changed by varying DO or DOC, respectively. Results presented are steady*
 425 *state for central dune at $t = 10$ days from the three-dune model domain (Figure 1).*

426

427 3.3.2 Spatial and Temporal Variation

428 We evaluated spatial and temporal trends at two example locations (top of the model domain,
 429 *X1*, and edge of the hyporheic flow cell, *X2*) for three different DO/DOC scenarios (base case

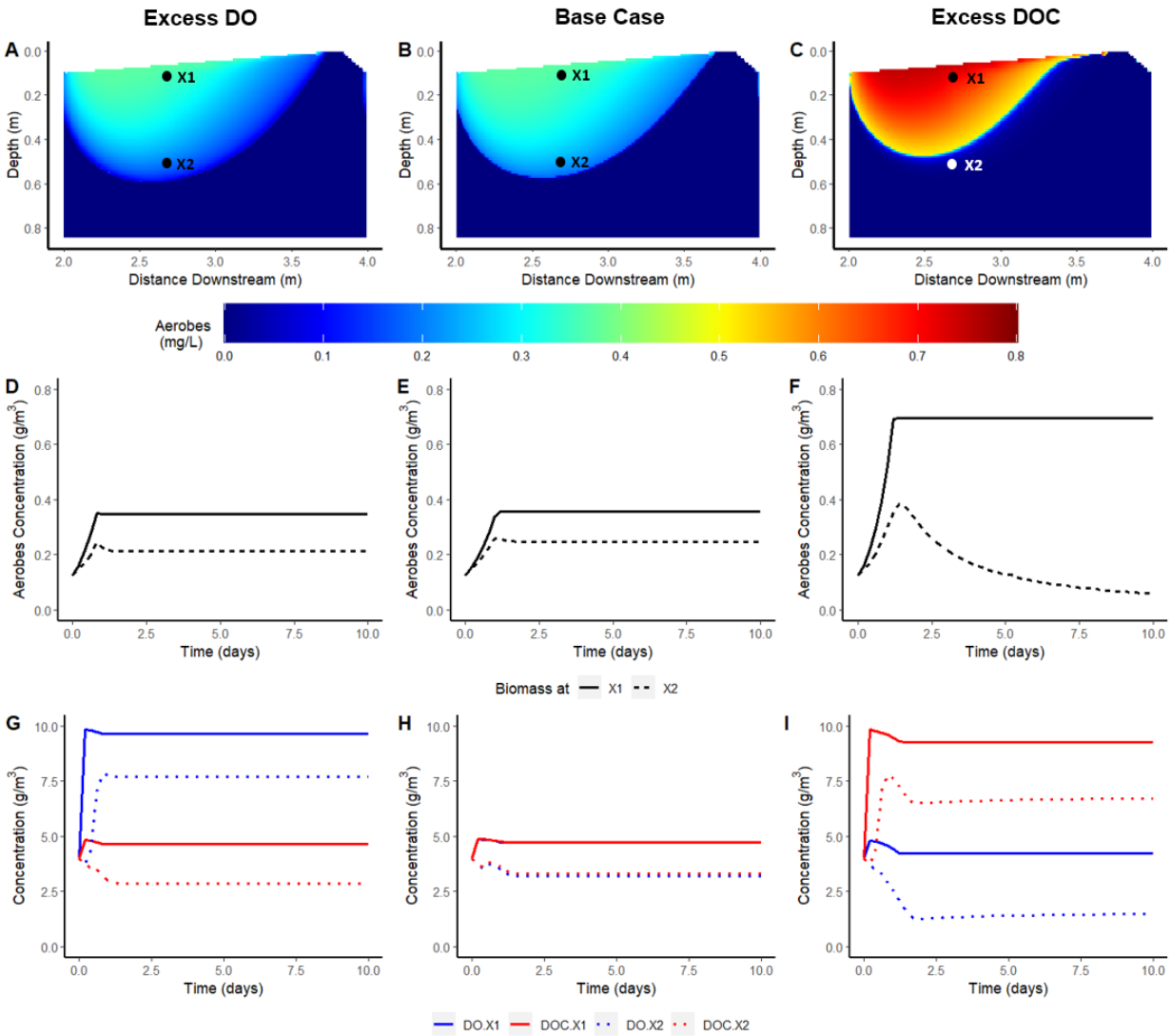
430 with equal SW DO and SW DOC concentrations, excess SW DO, and excess DOC)(Figure 10A,
431 B, C). *X1* ($x = 2.65$ m, depth = 0.15m) is located in a high DO and DOC concentration zone
432 close to the SW inflow boundary, while *X2* ($x = 2.65$ m, depth = 0.5 m) is located deeper in the
433 sediment, closer to the edge of the hyporheic flow cell area where DO and DOC concentrations
434 were lower.

435 Under excess SW DO, the spatial distribution of aerobic microbial biomass (Figure 10A) was
436 overall similar to that of the base case (Figure 10B). No significant differences in biomass were
437 observed between excess SW DO and the base case at any point in time at the top of the
438 hyporheic zone (*X1*), but biomass was slightly lower for excess SW DO at *X2* (Figure 10D, E).
439 By contrast, for excess SW DOC, microbial concentrations in the hyporheic zone were overall
440 significantly higher than for the base case, although the area in which microbes could subsist
441 decreased, i.e. microbial concentrations dropped to almost 0 mg/L at *X2* (Figure 10B, C).
442 Changes in both DO and DOC enhanced growth, but to different degrees.

443 Biomass response over time was different depending on the location within the dune and the top
444 boundary DO and DOC concentrations. For both excess DO and DOC, biomass increased
445 rapidly at *X1* with time and then suddenly leveled off (Figure 10D, E, F). By contrast, biomass at
446 *X2* showed a rapid initial increase with time and then at least some decrease thereafter (Figure
447 10D, E, F). This effect was by far the most pronounced with excess DOC, where biomass at *X2*
448 increased rapidly and then decreases rapidly again (Figure 10F).

449 All timeseries of DO and DOC concentrations eventually reached steady state (Figure 10D
450 through F). However, increasing either SW DO or DOC changed the time it took for DO and
451 DOC to reach steady state. For example, DO and DOC reached steady state in approximately 1
452 day for the base case (Figure 10H), and in 1.25 days or more when there was excess DOC
453 (Figure 10I). DO and DOC concentrations reached steady state in less than 2 days for all
454 modeled conditions, and steady state was reached earlier close to the core of the hyporheic flow
455 cell than it was at the edge of the cell (Figure 10D, E, F).

456

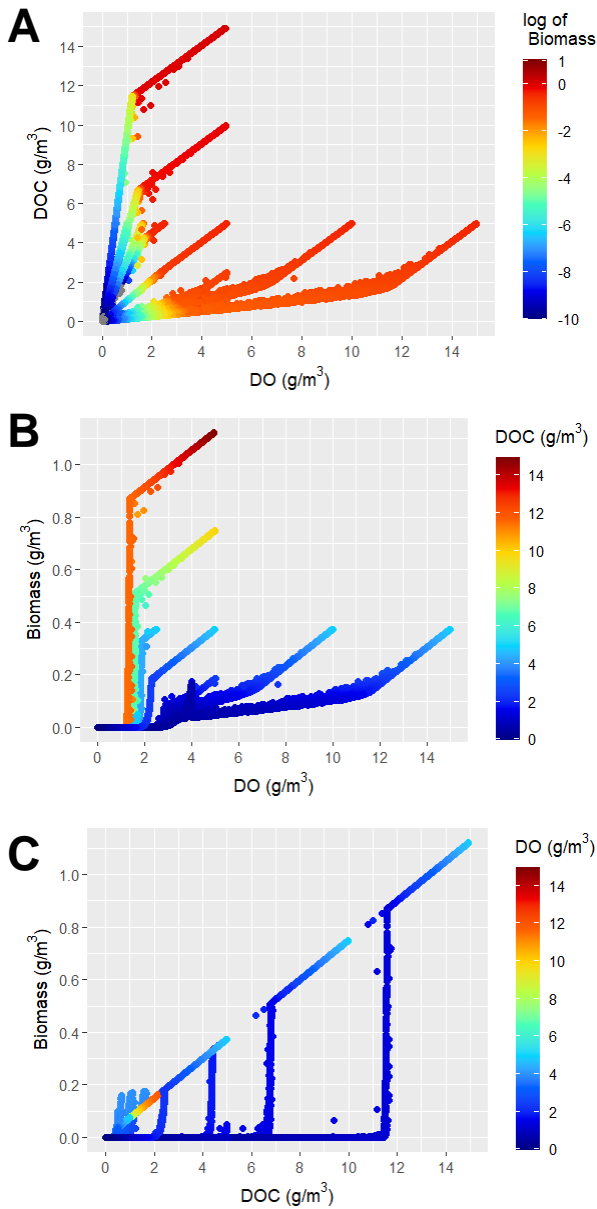


457

458 *Figure 10. Steady state ($t= 10$ days) spatial distribution of aerobic biomass concentration (with*
 459 *growth/death) for A) excess dissolved oxygen (DO) model (more top boundary DO than DOC,*
 460 *10 mg/L DO, 5 mg/L DOC), B) base Case (equal top boundary DO and DOC, 5 mg/L DO, 5*
 461 *mg/L DOC), and C) excess DOC model (more top boundary DOC than DO, 5mg/L DO, 10 mg/L*
 462 *DOC). Biomass time series for D) excess DO, E) base case, F) excess DOC. Concentration time*
 463 *series of DO and DOC for G) excess DO, H) base case and I) excess DOC. Solid lines represent*
 464 *point X1 while dotted and dashed lines represent point X2. Results presented are for central*
 465 *dune from the three-dune model domain (Figure 1).*

466

467 Microbial mass at steady state was nearly depleted in grid cells where DO concentrations were
468 less than $\sim 1 \text{ g/m}^3$ (Figure 11A). However, even in some cases with DO concentration above this
469 value, microbial mass was still depleted due to low DOC concentrations (Figure 11B). This
470 suggests that there are minimum DO and DOC concentrations required for microbial growth, but
471 they are not a specific absolute concentration or ratio of DO and DOC. These thresholds are
472 potentially related to the growth rate (G_b) which ultimately depends on the availability of EAs
473 and substrates (Equation 7). At some locations, DOC concentrations of up to 10 g/m^3 resulted in
474 a microbial mass concentration of $\sim 0 \text{ g/m}^3$ due to the low DO concentrations (Figure 11C;
475 Figure 10C, F, I).



476

477 *Figure 11. Steady-state ($t=10$ days) dissolved oxygen (DO), dissolved organic carbon (DOC),*
 478 *and biomass concentrations (with growth/death) for all model grid cells in all 12 concentration*
 479 *sensitivity analysis runs (Table 1). The dataset is presented multiple ways, including A) 3D plot,*
 480 *B) 2D plot with biomass as color scale, C) 2D plot with DOC as color scale, and D) 2D plot with*
 481 *DO as color scale. Results presented are for central dune from the three-dune model domain*
 482 *(Figure 1).*

483

484 **4. Discussion**

485 Our boundary DOC concentrations (1-15 mg/L, Table 1) were generally in the oligotrophic
486 range, leading to low simulated biomass concentrations that often did not exceed 0.8 g/m³
487 (Figures 3, 4, 7, 10), and never exceeded 1.2 g/m³ (Figure 11). This is consistent with other
488 studies of oligotrophic systems with generally low DOC and biomass and consequently minimal
489 to no bioclogging (De Falco et al. 2018, Ping et al. 2020, Xian et al. 2023).

490

491 **4.1 Importance of Simulating Microbial Growth/Death for Model Predictions**

492 Our results showed significant differences in total steady-state biomass (12% for the base case)
493 and its spatial distribution between the growth/death and no growth/no death scenarios (e.g.,
494 Figure 4). Similarly, there were noticeable differences in steady-state total DO and DOC mass
495 (up to 100%, Figure 8), and spatial distribution of DO and DOC concentration in the hyporheic
496 zone (e.g., Figure 10A, B, C). Furthermore, the fact that decreased microbial biomass in the
497 growth/death model was associated with decreased DO/DOC mass indicates that lower biomass
498 in the growth/death case was able to consume more DO/DOC (85% less at steady-state for the
499 base case), in turn suggesting greater efficiency of metabolism in the growth/death scenario.

500 This greater efficiency makes sense given biomass spatial distribution in the growth/death case is
501 allowed to adjust to spatial patterns of DO/DOC supply. Together, these findings emphasize the
502 importance of simulating microbial growth and death, and therefore the qualitative and
503 quantitative inaccuracy of ignoring microbial dynamics in models, if the predicted magnitude of
504 microbial biomass and by extension the predicted magnitudes of microbially-mediated
505 biogeochemical reactions (e.g., nitrification, denitrification) is important. Our results also
506 emphasize the importance of simulating microbial growth and death if the spatial distribution of
507 microbially-mediated reactions within the hyporheic zone (Figure 4) and their control by
508 hyporheic flowpaths (Figure 10, Section 4.2) are important (Mendoza-Lera et al. 2019). Prior
509 research has similarly found that simulating microbial growth/death can be important in other
510 ways such as where and when substrate (e.g., DOC) concentrations are sufficient to induce
511 bioclogging and associated reductions in sediment flow and reactant transport (Newcomer et al.
512 2016, Caruso et al. 2017, Xian et al. 2019, Ping et al. 2020).

513 By contrast, *trends* of steady state biomass and biomass concentration with hydraulic and
514 biochemical boundary conditions were similar for growth/death and no growth/no death

515 scenarios. For example, hyporheic zone DO and DOC increased with SW DO and SW DOC,
516 respectively, regardless of whether growth and death were simulated (Figure 5E). This suggests
517 that certain trends may be captured without modeling growth and death, but more research is
518 needed to determine how universal this conclusion is.

519 Explicitly simulating microbial growth and death also allows exploring and quantifying
520 biological response times to perturbations. Even with constant hydraulic and DO/DOC boundary
521 conditions, initial dynamic periods of microbial adjustment to current conditions and hence
522 adjustment of DO and DOC concentrations occurred (Figures 4, 10). These response times
523 varied widely from roughly 1-1.5 days for the base case (Figures 4GH, 10EH) to more than a
524 week for the excess DOC case (Figure 10F). Higher response times seem to be associated with
525 deeper locations (i.e. higher residence times, Section 4.2 below), but also more complex response
526 sequences when biological communities first grow and then die out (Figure 10F, location X2).
527 Such response times are likely playing out continually in the field, where hydrologic and
528 biogeochemical conditions are highly dynamic (see Section 4.3, below).

529

530 **4.2 Effect of DO/DOC Availability and Residence Times on Growth/Death**

531 Our results suggest that there are specific lower DO and DOC concentration thresholds required
532 for aerobic microbial growth and these concentrations are neither absolute minimums nor
533 specific DO:DOC ratios (e.g., Figure 11). This makes sense because the population growth rate
534 (G_b) increases with both the yield coefficient (Y) and the max specific rate of substrate utilization
535 (v^{max}) (Equation 5). Given that the half saturation concentration for DOC is greater than that for
536 DO, R_{DOC} increases more with DOC concentration than it does with DO. For example, a
537 DO:DOC ratio of 0.5 could be caused by a DOC concentration of 10 g/m³ and a DO
538 concentration of 5 g/m³, resulting in a specific substrate utilization rate of ~6.09 g/g/d. For a ratio
539 of 2.0, the values would be inverted (10 g/m³ of DO and 5 g/m³ of DOC) and the specific
540 substrate utilization rate would be 5.59 g/g/d. Even though these utilization rates are
541 approximately 10% different, this difference is still enough to compound over time to create the
542 differences observed in the sensitivity analysis.

543 Locations within the model domain with longer residence times (i.e. longer flow times from the
544 top boundary) had lower, or in some cases, mostly depleted aerobic microbial biomass (Figure

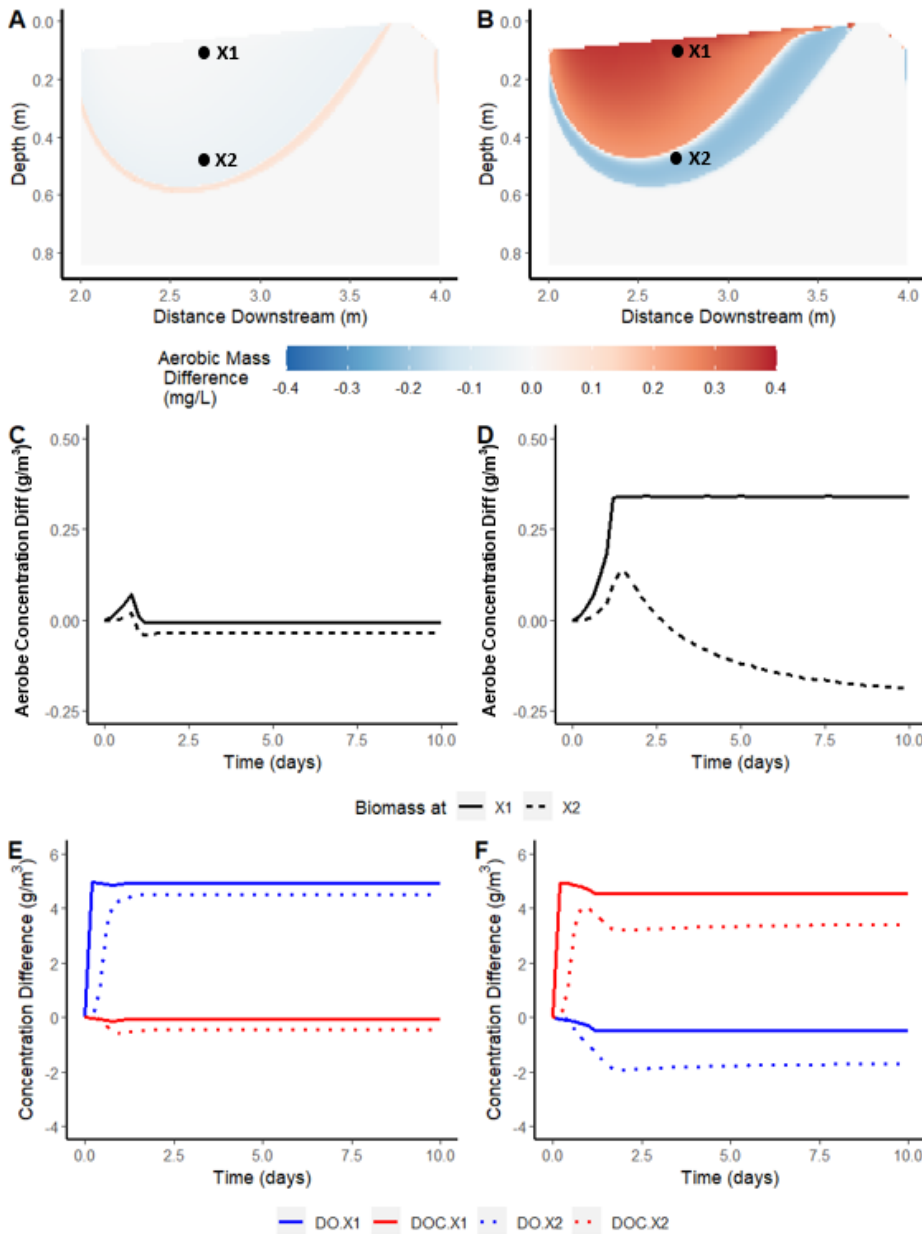
545 12B, D; Figure 7). This makes sense because biomass depends on the availability of DO and
546 DOC and locations with higher residence times mean longer travel times for DO and DOC from
547 the top boundary, and therefore greater depletion of these resources before arriving at that
548 particular location (Figure 4). For our scenarios, these locations with greater residence times are
549 generally deeper in the sediment, close to the edge of the hyporheic flow cell (Figure 10C, F).

550 Variation in residence times also explains the scatter in total aerobic microbial biomass as a
551 function of hyporheic flow cell area (Figure 5E). Different hydraulic conditions cause different
552 residence times and high residence times cause reduced DO and DOC which mostly depletes the
553 biomass (Figure 11C, 7A). Therefore, different dunes with the same hyporheic flow cell area
554 could result in different steady state total aerobic biomass if the hydraulic conditions and thus
555 porewater velocities, differ. However, minimum and maximum possible steady state biomasses
556 may exist for a given flow cell area, and these limits may increase with flow cell area.

557 The spatial pattern of deviations in aerobic microbial biomass concentration from the base case
558 differed between conditions of excess SW DO and those of excess SW DOC (Figure 12A, B).

559 The overall differences were less for excess SW DO than excess SW DOC, consistent with
560 Figure 10. The base case exceeded excess DOC only at the fringes of the hyporheic flow cell
561 whereas the base case exceeded excess DO throughout the core of the flow cell. Increasing SW
562 DO or SW DOC relative to the base case resulted in increased total biomass (Figure 12C, D, E,
563 F). Closer to the edge of the hyporheic flow cell (location X2), biomass reached its peak (~ 2
564 days) after DO and DOC (~ 1.5 days) and then started to decrease below the biomass
565 concentration of the base case (Figure 12D, E, F).

566



567

568 *Figure 12. Differences between excess dissolved oxygen (DO) and excess dissolved organic*
 569 *carbon (DOC) in top boundary surface water compared to base case for growth/death*
 570 *conditions (Left column corresponds to excess DO – base case and right column, excess DOC –*
 571 *base case). Spatial distribution of biomass difference for A) excess DO B) excess DOC at $t = 10$*
 572 *days. Biomass timeseries for C) excess DO and D) excess DOC. DO and DOC concentrations*
 573 *for E) excess DO and F) excess DOC. Solid lines represent point X1 while dotted and dashed*
 574 *lines represent point X2. Results presented are for central dune from the three-dune model*
 575 *domain (Figure 1).*

576

577 Ultimately, understanding biomass patterns over time and space requires understanding how DO
578 and DOC are transported to each grid cell by the GW flow paths through the hyporheic zone.
579 Each grid cell stores DO and DOC, which changes according to the mass balance of inflow,
580 outflow, and consumption by biomass. At $t = 0$ (t_0), the microbial population starts consuming
581 whatever DO and DOC is initially stored (initial concentrations), and DO and DOC is
582 continually transported to the cell along hyporheic flow paths. As long as DO and DOC are
583 available, the aerobes reproduce, and the microbial population keeps growing. In some cases the
584 microbial population eventually starts consuming more DO and DOC than the flow paths can
585 transport to their location and the storage at that grid cell starts depleting (Figure 10 D through I).
586 In most cases, inflow, outflow and consumption eventually balance out and steady state is
587 reached for biomass, DO, and DOC. However, in some cases, the storage drops to a point where
588 the minimum concentrations required for growth are not met (Figure 11), and biomass drops to
589 almost 0 g/m^3 (Figure 10I). Thus, distance along a flow path (residence time) and DO and DOC
590 availability play key roles in microbial growth and death dynamics in the hyporheic zone.

591 Note that we only simulated strict aerobes, and thus our results may be different if we had also
592 simulated other microbial populations, for example facultative microbes. If we added microbial
593 populations that can utilize other electron acceptors, that would allow utilization of any
594 remaining DOC in the system and allow DOC concentrations to further deplete in certain
595 scenarios relative to our results. This would require a significantly more complex model, to
596 account for differing growth and death responses with additional electron acceptors such as
597 nitrate. This area is recommended for future research.

598

599 **4.3 Temporal Variations in Hydraulic and DO/DOC Boundary Conditions**

600 Although each model scenario we ran had steady-state boundary conditions, river flow and depth
601 are constantly fluctuating due to natural (e.g., storms, tides, variation in snowmelt,
602 evapotranspiration) and anthropogenic (e.g., dam operation) causes (Lins 1985, Cohn and Lins
603 2005, Loheide and Lundquist 2009, Gomez-Velez et al. 2015, Malzone et al. 2016, Schmadel et
604 al. 2016, Knights et al. 2017). Nevertheless, we can gain some insight from our variation of
605 hydraulic and DO/DOC boundary conditions *among* model scenarios. For example, during

606 hydropower peaking, daily snowmelt, and high tides (Loheide and Lundquist 2009, Sawyer et al.
607 2009, Bianchin et al. 2011), SW head would increase, leading to larger hyporheic flow cells
608 (Azinheira et al. 2014) and larger hyporheic biomass (Figure 5). The reverse would then occur
609 during the other half of the diel cycle, with a lag between SW fluctuations and biological and
610 chemical response of approximately 1-6 hours. The specific trends discussed here depend on our
611 specific boundary conditions, i.e. DO and DOC both present in SW and neither present in deeper
612 GW. However, even with different DO/DOC boundary conditions, the more fundamental
613 findings such as delayed biomass response in the subsurface should still hold. This is a key
614 distinction from models that do not include microbial growth and death, where the delays would
615 only be from transport time along flowpaths, without the additional delay of biological response
616 times (Hester et al. 2019, Santizo et al. 2020, Hester et al. 2021).

617
618 Any fluctuations in biogeochemical boundary conditions would then be superimposed on the
619 effects of fluctuations in hydraulics. In our case, that would mean increases in boundary DO or
620 DOC would increase hyporheic biomass. Such variation in biogeochemical boundary conditions
621 may occur due to passage of storm events and seasons. For example, both DOC loads and
622 concentrations in stream and river channels can increase during storm events (Hinton et al. 1997,
623 Inamdar et al. 2004, Lindroth et al. 2009). SW organic carbon levels have also been found to be
624 higher in wet and/or growing seasons (Lee et al. 2016, Li et al. 2017b), and SW DO levels are
625 often higher during colder seasons due to higher solubility and less consumption by algae or
626 bacteria (He et al. 2011, Rajwa-Kuligiewicz et al. 2015).

627

628 **5. Conclusions**

629 We used MODFLOW and SEAM3D to simulate the effect of microbial growth and death
630 processes within riverbed dunes on hyporheic zone metabolism of dissolved oxygen (DO) and
631 dissolved organic carbon (DOC) derived from surface water (SW). Our results show that at
632 steady state conditions, the efficiency of metabolic processes can increase when microbes,
633 through growth and death processes, can optimize their spatial distribution to take advantage of
634 heterogeneous patterns of DO/DOC availability. Thus, modeling growth and death in microbial
635 populations is necessary for accurate simulation of microbially-mediated reactions in the
636 hyporheic zone. This would be particularly true where environmental conditions such as

637 temperature, reactant concentrations, and hydraulic conductivity vary temporally or spatially.
638 Because hyporheic reactions can significantly affect water quality of the overlying water column
639 (*Gomez-Velez et al.*, 2015), this has implications for quantifying beneficial reactions and
640 therefore watershed water quality management. It is true that some general trends can be
641 captured without modeling microbial growth and death, particularly those trends driven primarily
642 by hydraulic or chemical boundary conditions. Yet accuracy of simulated concentration or
643 reaction magnitudes are improved by explicitly simulating microbial growth and death. This is
644 particularly true of modeling studies that require accurate predictions of spatial distribution of
645 electron acceptors and substrates.

646

647

648 **Acknowledgements**

649

650 Funding: This work was supported by the U.S. Department of Energy [grant number DE-
651 SC0021402].

652

653 **References**

- 654 Azinheira, D. L., D. T. Scott, W. C. Hession, and E. T. Hester. 2014. Comparison of effects of
655 inset floodplains and hyporheic exchange induced by in-stream structures on solute
656 retention. *Water Resources Research* **50**:6168-6190.
- 657 Bardini, L., F. Boano, M. B. Cardenas, R. Revelli, and L. Ridolfi. 2012. Nutrient cycling in
658 bedform induced hyporheic zones. *Geochimica Et Cosmochimica Acta* **84**:47-61.
- 659 Best, J., and R. Kostaschuk. 2002. An experimental study of turbulent flow over a low-angle
660 dune. *Journal of Geophysical Research-Oceans* **107**.
- 661 Bianchin, M. S., L. Smith, and R. D. Beckie. 2011. Defining the hyporheic zone in a large tidally
662 influenced river. *Journal of Hydrology* **406**:16-29.
- 663 Bradley, R. W., and J. G. Venditti. 2019. The Growth of Dunes in Rivers. *Journal of*
664 *Geophysical Research-Earth Surface* **124**:548-566.
- 665 Cardenas, M. B. 2009. Stream-aquifer interactions and hyporheic exchange in gaining and losing
666 sinuous streams. *Water Resources Research* **45**.
- 667 Cardenas, M. B. 2015. Hyporheic zone hydrologic science: A historical account of its emergence
668 and a prospectus. *Water Resources Research* **51**:3601-3616.
- 669 Cardenas, M. B., and J. L. Wilson. 2006. The influence of ambient groundwater discharge on
670 exchange zones induced by current-bedform interactions. *Journal of Hydrology* **331**:103-
671 109.

672 Cardenas, M. B., and J. L. Wilson. 2007. Hydrodynamics of coupled flow above and below a
673 sediment-water interface with triangular bedforms. *Advances in Water Resources* **30**:301-
674 313.

675 Caruso, A., F. Boano, L. Ridolfi, D. L. Chopp, and A. Packman. 2017. Biofilm-induced
676 bioclogging produces sharp interfaces in hyporheic flow, redox conditions, and microbial
677 community structure. *Geophysical Research Letters* **44**:4917-4925.

678 Cisneros, J., J. Best, T. van Dijk, R. P. de Almeida, M. Amsler, J. Boldt, B. Freitas, C. Galeazzi,
679 R. Huizinga, M. Ianniruberto, H. B. Ma, J. A. Nittrouer, K. Oberg, O. Orfeo, D. Parsons,
680 R. Szupiany, P. Wang, and Y. F. Zhang. 2020. Dunes in the world's big rivers are
681 characterized by low-angle lee-side slopes and a complex shape. *Nature Geoscience*
682 **13**:156-+.

683 Cohn, T. A., and H. F. Lins. 2005. Nature's style: Naturally trendy. *Geophysical Research Letters*
684 **32**.

685 Colombini, M., and A. Stocchino. 2008. Finite-amplitude river dunes. *Journal Of Fluid*
686 *Mechanics* **611**:283-306.

687 Cook, S., O. Price, A. King, C. Finnegan, R. van Egmond, H. Schafer, J. M. Pearson, S.
688 Abolfathi, and G. D. Bending. 2020. Bedform characteristics and biofilm community
689 development interact to modify hyporheic exchange. *Science of the Total Environment*
690 **749**.

691 Corsi, S. R., R. D. Klaper, D. N. Weber, and R. T. Bannerman. 2011. Water- and sediment-
692 quality effects on Pimephales promelas spawning vary along an agriculture-to-urban
693 land-use gradient. *Science of the Total Environment* **409**:4847-4857.

694 De Falco, N., F. Boano, A. Bogler, E. Bar-Zeev, and S. Arnon. 2018. Influence of Stream-
695 Subsurface Exchange Flux and Bacterial Biofilms on Oxygen Consumption Under
696 Nutrient-Rich Conditions. *Journal of Geophysical Research-Biogeosciences* **123**:2021-
697 2034.

698 Dubrovsky, N. M., K. R. Burow, G. M. Clark, J. Gronberg, P. A. Hamilton, K. J. Hitt, D. K.
699 Mueller, M. D. Munn, B. T. Nolan, and L. J. Puckett. 2010. The Quality of Our Nation's
700 Water: Nutrients in the Nation's Streams and Groundwater, 1992-2004. USGS Circular
701 1350. US Department of the Interior, US Geological Survey.

702 Elliott, A. H., and N. H. Brooks. 1997. Transfer of nonsorbing solutes to a streambed with bed
703 forms: Theory. *Water Resources Research* **33**:123-136.

704 Essaid, H. I., B. A. Bekins, E. M. Godsy, E. Warren, M. J. Baedeker, and I. M. Cozzarelli.
705 1995. Simulation of aerobic and anaerobic biodegradation processes at a crude oil spill
706 site. *Water Resources Research* **31**:3309-3327.

707 Fehlman, H. M. 1985. Resistance components and velocity distributions of open channel flows
708 over bedforms. Colorado State University, Fort Collins, CO.

709 Findlay, S. 2000. Microbial communities in hyporheic sediments. Pages 287-306 in J. Jones and
710 P. J. Mulholland, editors. *Streams and Ground Waters*.

711 Galloway, J., A. Fox, J. Lewandowski, and S. Arnon. 2019. The effect of unsteady streamflow
712 and stream-groundwater interactions on oxygen consumption in a sandy streambed.
713 *Scientific Reports* **9**.

714 Gomez-Velez, J., and J. W. Harvey. 2014. A hydrogeomorphic river network model predicts
715 where and why hyporheic exchange is important in large basins. *Geophysical Research*
716 *Letters* **41**:6403-6412.

717 Gomez-Velez, J. D., J. Harvey, M. B. Cardenas, and B. Kiel. 2015. Denitrification in the
718 Mississippi River network controlled by flow through river bedforms. *Nature Geoscience*
719 **8**:941-U975.

720 Gooseff, M. N. 2010. Defining hyporheic zones – Advancing our conceptual and operational
721 definitions of where stream water and groundwater meet. *Geography Compass* **4**:945-
722 955.

723 Harbaugh, A. W. 2005. MODFLOW-2005, the U.S. Geological Survey modular ground-water
724 model -- the Ground-Water Flow Process: U.S. Geological Survey Techniques and
725 Methods 6-A16. U.S. Geological Survey, Reston, VA.

726 He, J., A. Chu, M. C. Ryan, C. Valeo, and B. Zaitlin. 2011. Abiotic influences on dissolved
727 oxygen in a riverine environment. *Ecological Engineering* **37**:1804-1814.

728 Hendricks, S. P., and D. S. White. 1991. Physicochemical Patterns within a Hyporheic Zone of a
729 Northern Michigan River, with Comments on Surface-Water Patterns. *Canadian Journal*
730 *of Fisheries and Aquatic Sciences* **48**:1645-1654.

731 Hester, E. T., K. E. Brooks, and D. T. Scott. 2018. Comparing reach scale hyporheic exchange
732 and denitrification induced by instream restoration structures and natural streambed
733 morphology. *Ecological Engineering* **115**:105-121.

734 Hester, E. T., and M. W. Doyle. 2008. In-stream geomorphic structures as drivers of hyporheic
735 exchange. *Water Resources Research* **44**:W03417.

736 Hester, E. T., L. E. Eastes, and M. A. Widdowson. 2019. Effect of Surface Water Stage
737 Variation on Mixing-Dependent Hyporheic Denitrification in Riverbed Dunes. *Water*
738 *Resources Research* **55**:4668-4687.

739 Hester, E. T., K. Y. Santizo, A. A. Nida, and M. A. Widdowson. 2021. Hyporheic transverse
740 mixing zones and dispersivity: Laboratory and numerical experiments of hydraulic
741 controls. *Journal of Contaminant Hydrology* **243**:103885.

742 Hester, E. T., K. I. Young, and M. A. Widdowson. 2013. Mixing of surface and groundwater
743 induced by riverbed dunes: implications for hyporheic zone definitions and pollutant
744 reactions. *Water Resources Research* **49**:5221-5237.

745 Hester, E. T., K. I. Young, and M. A. Widdowson. 2014. Controls on mixing-dependent
746 denitrification in hyporheic zones induced by riverbed dunes: A steady state modeling
747 study. *Water Resources Research* **50**:9048-9066.

748 Hinton, M. J., S. L. Schiff, and M. C. English. 1997. The significance of storms for the
749 concentration and export of dissolved organic carbon from two Precambrian Shield
750 catchments. *Biogeochemistry* **36**:67-88.

751 Inamdar, S. P., S. F. Christopher, and M. J. Mitchell. 2004. Export mechanisms for dissolved
752 organic carbon and nitrate during summer storm events in a glaciated forested catchment
753 in New York, USA. *Hydrological Processes* **18**:2651-2661.

754 Jones, J. B., and P. J. Mulholland. 2000. *Streams and ground waters*. Academic Press, San
755 Diego, CA.

756 Kaufman, M. H., M. B. Cardenas, J. Buttles, A. J. Kessler, and P. L. M. Cook. 2017. Hyporheic
757 hot moments: Dissolved oxygen dynamics in the hyporheic zone in response to surface
758 flow perturbations. *Water Resources Research* **53**:6642-6662.

759 Kessler, A. J., R. N. Glud, M. B. Cardenas, and P. L. M. Cook. 2013. Transport zonation limits
760 coupled nitrification-denitrification in permeable sediments. *Environmental Science &*
761 *Technology* **47**:13404-13411.

762 Knights, D., A. H. Sawyer, R. T. Barnes, C. T. Musial, and S. Bray. 2017. Tidal controls on
763 riverbed denitrification along a tidal freshwater zone. *Water Resources Research* **53**:799-
764 816.

765 Lee, J., K. Shin, C. Park, S. Lee, D. R. Jin, Y. Kim, and S. Yu. 2016. Spatial and seasonal
766 variations of organic carbon level in four major rivers in Korea. *Environmental*
767 *Engineering Research* **21**:84-90.

768 Li, A., A. F. Aubeneau, D. Bolster, J. L. Tank, and A. I. Packman. 2017a. Covariation in patterns
769 of turbulence-driven hyporheic flow and denitrification enhances reach-scale nitrogen
770 removal. *Water Resources Research* **53**:6927–6944

771 Li, B., X. F. Liu, M. H. Kaufman, A. Turetaia, X. Y. Chen, and M. B. Cardenas. 2020. Flexible
772 and Modular Simultaneous Modeling of Flow and Reactive Transport in Rivers and
773 Hyporheic Zones. *Water Resources Research* **56**.

774 Li, X.-y., Y.-j. Ding, T.-d. Han, J.-z. Xu, S.-c. Kang, Q.-b. Wu, M. Sillanpaa, Z.-b. Yu, and C.-r.
775 Yu. 2017b. Seasonal variations of organic carbon and nitrogen in the upper basins of
776 Yangtze and Yellow Rivers. *Journal of Mountain Science* **14**:1577-1590.

777 Lindroth, A., F. Lagergren, A. Grelle, L. Klemedtsson, O. Langvall, P. Weslien, and J. Tuulik.
778 2009. Storms can cause Europe-wide reduction in forest carbon sink. *Global Change*
779 *Biology* **15**:346-355.

780 Lins, H. F. 1985. STREAMFLOW VARIABILITY IN THE UNITED-STATES - 1931-78.
781 *Journal of Climate and Applied Meteorology* **24**:463-471.

782 Loheide, S. P., and J. D. Lundquist. 2009. Snowmelt-induced diel fluxes through the hyporheic
783 zone. *Water Resources Research* **45**:W07404.

784 Lotts, W. S. 2022. In the zone: the effects of soil pipes and dunes on hyporheic and riparian zone
785 hydraulics and biogeochemistry. Virginia Tech, Blacksburg, VA.

786 Malzone, J. M., S. K. Anseeuw, C. S. Lowry, and R. Allen-King. 2016. Temporal Hyporheic
787 Zone Response to Water Table Fluctuations. *Groundwater* **54**:274-285.

788 Mendoza-Lera, C., A. Frossard, M. Knie, L. L. Federlein, M. O. Gessner, and M. Mutz. 2017.
789 Importance of advective mass transfer and sediment surface area for streambed microbial
790 communities. *Freshwater Biology* **62**:133-145.

791 Mendoza-Lera, C., M. Ribot, A. Foulquier, E. Marti, C. Bonnineau, P. Breil, and T. Datry. 2019.
792 Exploring the role of hydraulic conductivity on the contribution of the hyporheic zone to
793 in-stream nitrogen uptake. *Ecohydrology* **12**.

794 Molz, F. J., M. A. Widdowson, and L. D. Benefield. 1986. SIMULATION OF MICROBIAL-
795 GROWTH DYNAMICS COUPLED TO NUTRIENT AND OXYGEN-TRANSPORT
796 IN POROUS-MEDIA. *Water Resources Research* **22**:1207-1216.

797 Newcomer, M. E., S. S. Hubbard, J. H. Fleckenstein, U. Maier, C. Schmidt, M. Thullner, C.
798 Ulrich, N. Flipo, and Y. Rubin. 2016. Simulating bioclogging effects on dynamic
799 riverbed permeability and infiltration. *Water Resources Research* **52**:2883-2900.

800 Nogaro, G., T. Datry, F. Mermillod-Blondin, A. Foulquier, and B. Montuelle. 2013. Influence of
801 hyporheic zone characteristics on the structure and activity of microbial assemblages.
802 *Freshwater Biology* **58**:2567-2583.

803 Ping, X., M. Jin, and Y. Xian. 2020. Effect of bioclogging on the nitrate source and sink function
804 of a hyporheic zone. *Journal of Hydrology* **590**.

805 Ping, X., Y. Xian, and M. G. Jin. 2022. Influence of Bedform Migration on Nitrate Reduction in
806 Hyporheic Zones of Heterogeneous Sediments. *Water Resources Research* **58**.

807 Pollock, D. W. 2012. User guide for MODPATH version 6: a particle tracking model for
808 MODFLOW (p. 58). US: US Department of the Interior, US Geological Survey.

809 Rajwa-Kuligiewicz, A., R. J. Bialik, and P. M. Rowinski. 2015. Dissolved oxygen and water
810 temperature dynamics in lowland rivers over various timescales. *Journal of Hydrology*
811 and *Hydromechanics* **63**:353-363.

812 Santizo, K. Y., M. A. Widdowson, and E. T. Hester. 2020. Abiotic mixing-dependent reaction in
813 a laboratory simulated hyporheic zone. *Water Resources Research* **56**:e2020WR027090.

814 Sawyer, A. H., M. B. Cardenas, A. Bomar, and M. Mackey. 2009. Impact of dam operations on
815 hyporheic exchange in the riparian zone of a regulated river. *Hydrological Processes*
816 **23**:2129-2137.

817 Schmadel, N. M., A. S. Ward, C. S. Lowry, and J. M. Malzone. 2016. Hyporheic exchange
818 controlled by dynamic hydrologic boundary conditions. *Geophysical Research Letters*
819 **43**:4408-4417.

820 Singh, T., L. W. Wu, J. D. Gomez-Velez, J. Lewandowski, D. M. Hannah, and S. Krause. 2019.
821 Dynamic Hyporheic Zones: Exploring the Role of Peak Flow Events on Bedform-
822 Induced Hyporheic Exchange. *Water Resources Research* **55**:218-235.

823 Stegen, J. C., J. K. Fredrickson, M. J. Wilkins, A. E. Konopka, W. C. Nelson, E. V. Arntzen, W.
824 B. Chrisler, R. K. Chu, R. E. Danczak, S. J. Fansler, D. W. Kennedy, C. T. Resch, and M.
825 Tfaily. 2016. Groundwater-surface water mixing shifts ecological assembly processes
826 and stimulates organic carbon turnover. *Nature Communications* **7**.

827 Stegen, J. C., T. Johnson, J. K. Fredrickson, M. J. Wilkins, A. E. Konopka, W. C. Nelson, E. V.
828 Arntzen, W. B. Chrisler, R. K. Chu, S. J. Fansler, E. B. Graham, D. W. Kennedy, C. T.
829 Resch, M. Tfaily, and J. Zachara. 2018. Influences of organic carbon speciation on
830 hyporheic corridor biogeochemistry and microbial ecology. *Nature Communications* **9**.

831 Sun, R. K., J. W. Dong, Y. Li, P. W. Li, Y. N. Liu, Y. Liu, and J. H. Feng. 2022. The Influence
832 Research on Nitrogen Transport and Reaction in the Hyporheic Zone with an In-Stream
833 Structure. *International Journal of Environmental Research and Public Health* **19**.

834 Waddill, D. W., and M. A. Widdowson. 1998. Three-dimensional model for subsurface transport
835 and biodegradation. *Journal of Environmental Engineering-Asce* **124**:336-344.

836 Waddill, D. W., and M. A. Widdowson. 2000. SEAM3D: A numerical model for three-
837 dimensional solute transport and sequential electron acceptor-based bioremediation in
838 groundwater. ERDC/EL TR-00-18, U.S. Army Engineer Research and Development
839 Center, Vicksburg, MS, 89 pp.

840 Weller, H. G., G. Tabor, H. Jasak, and C. Fureby. 1998. A tensorial approach to computational
841 continuum mechanics using object-oriented techniques. *Computers in Physics* **12**:620-
842 631.

843 Widdowson, M. A., F. J. Molz, and L. D. Benefield. 1988. A NUMERICAL TRANSPORT
844 MODEL FOR OXYGEN-BASED AND NITRATE-BASED RESPIRATION LINKED
845 TO SUBSTRATE AND NUTRIENT AVAILABILITY IN POROUS-MEDIA. *Water*
846 *Resources Research* **24**:1553-1565.

847 Wolke, P., Y. Teitelbaum, C. Deng, J. Lewandowski, and S. Arnon. 2020. Impact of Bed Form
848 Celerity on Oxygen Dynamics in the Hyporheic Zone. *Water* **12**:62.

849 Xian, Y., M. Jin, H. Zhan, and Y. Liu. 2019. Reactive Transport of Nutrients and Bioclogging
850 During Dynamic Disconnection Process of Stream and Groundwater. *Water Resources*
851 *Research* **55**:3882-3903.

852 Xian, Y., Z. Wen, M. G. Jin, X. Liang, and H. Jakada. 2023. Groundwater-borne nitrate removal
853 within heterogeneous sediments under interactions between hydraulics, nutrients, and
854 biofilms. *Journal of Hydrology* **616**.

- 855 Zarnetske, J. P., R. Haggerty, S. M. Wondzell, V. A. Bokil, and R. Gonzalez-Pinzon. 2012.
856 Coupled transport and reaction kinetics control the nitrate source-sink function of
857 hyporheic zones. *Water Resources Research* **48**:W11508.
- 858 Zheng, L. Z., and M. B. Cardenas. 2018. Diel Stream Temperature Effects on Nitrogen Cycling
859 in Hyporheic Zones. *Journal of Geophysical Research-Biogeosciences* **123**:2743-2760.

860

861